Earthquake scaling relations for mid-ocean ridge transform faults

M. S. Boettcher

Marine Geology and Geophysics, MIT/WHOI Joint Program, Woods Hole, Massachusetts, USA

T. H. Jordan

Department of Earth Sciences, University of Southern California, Los Angeles, California, USA

Received 24 March 2004; revised 8 July 2004; accepted 30 July 2004; published 9 December 2004.

[1] A mid-ocean ridge transform fault (RTF) of length L, slip rate V, and moment release rate $\dot{M}$ can be characterized by a seismic coupling coefficient $\chi = A_E/A_T$, where $A_E \sim \dot{M}/V$ is an effective seismic area and $A_T \propto L^{3/2}V^{-1/2}$ is the area above an isotherm T_{ref}. A global set of 65 RTFs with a combined length of 16,410 km is well described by a linear scaling relation (1) $A_E \propto A_T$, which yields $\chi = 0.15 \pm 0.05$ for $T_{ref} = 600°C$. Therefore about 85% of the slip above the 600°C isotherm must be accommodated by subseismic mechanisms, and this slip partitioning does not depend systematically on either V or L. RTF seismicity can be fit by a truncated Gutenberg-Richter distribution with a slope $\beta = 2/3$ in which the cumulative number of events N_0 and the upper cutoff moment $M_C = \mu D_C A_C$ depend on A_T. Data for the largest events are consistent with a self-similar slip scaling, $D_C \propto A_C^{1/2}$, and a square root areal scaling (2) $A_C \propto A_T^{1/2}$. If relations 1 and 2 apply, then moment balance requires that the dimensionless seismic productivity, $\nu_0 \propto \dot{N}_0/A_T V$, should scale as $\nu_0 \propto A_T^{-1/4}$, which we confirm using small events. Hence the frequencies of both small and large earthquakes adjust with A_T to maintain constant coupling. RTF scaling relations appear to violate the single-mode hypothesis, which states that a fault patch is either fully seismic or fully aseismic and thus implies $A_C \leq A_E$. The heterogeneities in the stress distribution and fault structure responsible for relation 2 may arise from a thermally regulated, dynamic balance between the growth and coalescence of fault segments within a rapidly evolving fault zone. *INDEX TERMS:* 7230 Seismology: Seismicity and seismotectonics; 8123 Tectonophysics: Dynamics, seismotectonics; 8150 Tectonophysics: Plate boundary—general (3040); 3035 Marine Geology and Geophysics: Midocean ridge processes; *KEYWORDS:* earthquakes, scaling relations, fault mechanics

Citation: Boettcher, M. S., and T. H. Jordan (2004), Earthquake scaling relations for mid-ocean ridge transform faults, *J. Geophys. Res.*, *109*, B12302, doi:10.1029/2004JB003110.

1. Introduction

[2] How slip is accommodated on major faults remains a central problem of tectonics. Although synoptic models of fault slip behavior have been constructed [e.g., *Sibson*, 1983; *Yeats et al.*, 1997; *Scholz*, 2002], a full dynamical theory is not yet available. Some basic observational issues are (1) the partitioning of fault slip into seismic and aseismic components, including the phenomenology of steady creep [*Schulz et al.*, 1982; *Wesson*, 1988], creep transients (silent earthquakes) [*Sacks et al.*, 1978; *Linde et al.*, 1996; *Heki et al.*, 1997; *Hirose et al.*, 1999; *Dragert et al.*, 2001; *Miller et al.*, 2002], and slow earthquakes [*Kanamori and Cipar*, 1974; *Okal and Stewart*, 1982; *Beroza and Jordan*, 1990]; (2) the scaling of earthquake slip with rupture dimensions, e.g., for faults with large aspect ratios, whether slip scales with rupture width [*Romanowicz*, 1992, 1994; *Romanowicz and Ruff*, 2002], length [*Scholz*, 1994a, 1994b; *Hanks and Bakun*, 2002], or something in between [*Mai and Beroza*, 2000; P. Somerville, personal communication, 2003]; (3) the outer scale of faulting, i.e., the relationship between fault dimension and the size of the largest earthquake [*Jackson*, 1996; *Schwartz*, 1996; *Ward*, 1997; *Kagan and Jackson*, 2000]; (4) the effects of cumulative offset on shear localization and the frequency-magnitude statistics of earthquakes, in particular, characteristic earthquake behavior [*Schwartz and Coppersmith*, 1984; *Wesnousky*, 1994; *Kagan and Wesnousky*, 1996]; and (5) the relative roles of dynamic and rheologic (quenched) structures in generating earthquake complexity (Gutenberg-Richter statistics, Omori's Law) and maintaining stress heterogeneity [*Rice*, 1993; *Langer et al.*, 1996; *Shaw and Rice*, 2000].

[3] A plausible strategy for understanding these phenomena is to compare fault behaviors in different tectonic environments. Continental strike-slip faulting, where the

0148-0227/04/2004JB003110$09.00

observations are most comprehensive, provides a good baseline. Appendix A summarizes one interpretation of the continental data, which we will loosely refer to as the "San Andreas Fault (SAF) model," because it owes much to the abundant information from that particular fault system. Our purpose is not to support this particular interpretation (some of its features are clearly simplistic and perhaps wrong) but to use it as a means for contrasting the behavior of strike-slip faults that offset two segments of an oceanic spreading center. These ridge transform faults (RTFs) are the principal subject of our study.

[4] RTFs are known to have low seismic coupling on average [*Brune*, 1968; *Davies and Brune*, 1971; *Frohlich and Apperson*, 1992; *Okal and Langenhorst*, 2000]. Much of the slip appears to occur aseismically, and it is not clear which parts of the RTFs, if any, are fully coupled [*Bird et al.*, 2002]. Given the length and linearity of many RTFs, the earthquakes they generate tend to be rather small; since 1976, only one event definitely associated with an RTF has exceeded a moment-magnitude (m_W) of 7.0 (Harvard Centroid-Moment Tensor Project, 1976–2002, available at http://www.seismology.harvard.edu/projects/CMT) (Harvard CMT). Slow earthquakes are common on RTFs [*Kanamori and Stewart*, 1976; *Okal and Stewart*, 1982; *Beroza and Jordan*, 1990; *Ihmlé and Jordan*, 1994]. Many slow earthquakes appear to have a compound mechanism comprising both an ordinary (fast) earthquake and an infraseismic event with an anomalously low rupture velocity (quiet earthquake); in some cases, the infraseismic event precedes, and apparently initiates, the fast rupture [*Ihmlé et al.*, 1993; *Ihmlé and Jordan*, 1994; *McGuire et al.*, 1996; *McGuire and Jordan*, 2000]. Although the latter inference remains controversial [*Abercrombie and Ekström*, 2001, 2003], the slow precursor hypothesis is also consistent with episodes of coupled seismic slip observed on adjacent RTFs [*McGuire et al.*, 1996; *McGuire and Jordan*, 2000; *Forsyth et al.*, 2003].

[5] The differences observed for RTFs and continental strike-slip faults presumably reflect their tectonic environments. When examined on the fault scale, RTFs reveal many of the same complexities observed in continental systems: segmentation, braided strands, stepovers, constraining and releasing bends, etc. [*Pockalny et al.*, 1988; *Embley and Wilson*, 1992; *Yeats et al.*, 1997; *Ligi et al.*, 2002]. On a plate tectonic scale, however, RTFs are generally longer lived structures with cumulative displacements that far exceed their lengths, as evidenced by the continuity of ocean-crossing fracture zones [e.g., *Cande et al.*, 1989]. Moreover, the compositional structure of the oceanic lithosphere is more homogeneous, and its thermal structure is more predictable from known plate kinematics [*Turcotte and Schubert*, 2001]. Owing to the relative simplicity of the mid-ocean environment, RTF seismicity may therefore be more amenable to interpretation in terms of the dynamics of faulting and less contingent on its geologic history.

[6] In this paper, we investigate the phenomenology of oceanic transform faulting by constructing scaling relations for RTF seismicity. As in many other published studies, we focus primarily on earthquake catalogs derived from teleseismic data. Because there is a rich literature on the subject, we begin with a detailed review of what has been previously learned and express the key results in a consistent mathematical notation (see notation section). We then proceed with our own analysis, in which we derive new scaling relations based on areal measures of faulting. We conclude by using these relations to comment on the basic issues laid out in this introduction.

2. Background

[7] Oceanic and continental earthquakes provide complementary information about seismic processes. On the one hand, RTFs are more difficult to study than continental strike-slip earthquakes because they are farther removed from seismic networks; only events of larger magnitude can be located, and their source parameters are more poorly determined. On the other hand, the most important tectonic parameters are actually better constrained, at least on a global basis. An RTF has a well-defined length L, given by the distance between spreading centers, and a well-determined slip rate V, given by present-day plate motions. Moreover, the thermal structure of the oceanic lithosphere near spreading centers is well described by isotherms that deepen according to the square root of age.

[8] *Brune* [1968] first recognized that the average rate of seismic moment release could be combined with L and V to determine the effective thickness (width) of the seismic zone, W_E. For each earthquake in a catalog of duration Δt_{cat}, he converted surface wave magnitude m_S into seismic moment M and summed over all events to obtain the cumulative moment ΣM. Knowing that M divided by the shear modulus μ equals rupture area times slip, he obtained a formula for the effective seismic width

$$W_E = \frac{\Sigma M}{\mu L V \Delta t_{cat}}. \quad (1)$$

In his preliminary analysis, *Brune* [1968] found values of W_E in the range 2–7 km. A number of subsequent authors have applied Brune's procedure to direct determinations of M as well as to m_S catalogs [*Davies and Brune*, 1971; *Burr and Solomon*, 1978; *Solomon and Burr*, 1979; *Hyndman and Weichert*, 1983; *Kawaski et al.*, 1985; *Frohlich and Apperson*, 1992; *Sobolev and Rundquist*, 1999; *Okal and Langenhorst*, 2000; *Bird et al.*, 2002]. The data show considerable scatter with the effective seismic widths for individual RTFs varying from 0.1 to 8 km.

[9] Most studies agree that W_E increases with L and decreases with V, but the form of the scaling remains uncertain. Consider the simple, well-motivated hypothesis that the effective width is thermally controlled, which appeared in the literature soon after quantitative thermal models of the oceanic lithosphere were established [e.g., *Burr and Solomon*, 1978; *Kawaski et al.*, 1985]. If the seismic thickness corresponds to an isotherm, then it should deepen as the square root of lithospheric age, implying $W_E \propto L^{1/2}V^{-1/2}$ and $\Sigma M \propto L^{3/2}V^{1/2}$ [e.g., *Okal and Langenhorst*, 2000]. However, two recent studies have suggested that W_E instead scales exponentially with V [*Frohlich and Apperson*, 1992; *Bird et al.*, 2002], while another proposes that ΣM scales exponentially with L [*Sobolev and Rundquist*, 1999]. The most recent papers, by *Langenhorst and Okal* [2002] and *Bird et al.* [2002], do not explicitly test the thermal scaling of W_E.

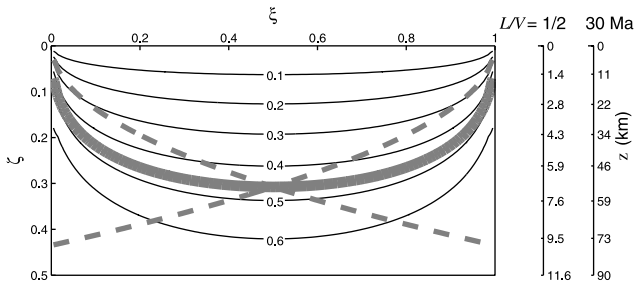

Figure 1. Thermal area of contact, A_T, is the fault area above a reference isotherm T_{ref}. Temperatures of the plates bounding the fault are assumed to evolve as $T_0\,\mathrm{erf}[\zeta\xi^{-1/2}]$ and $T_0\,\mathrm{erf}[\zeta(1-\xi)^{-1/2}]$, where T_0 is the mantle potential temperature, $\xi = x/L$ and $\zeta = 2/\sqrt{8\kappa L/V}$ are nondimensionalized length and depth, and κ is the thermal diffusivity. Fault isotherms T/T_0 (thin curves) are calculated by averaging the two plate temperatures, which reach a maximum depth in kilometers at $z_{max} = 2\sqrt{\kappa L/V}\,\mathrm{erf}^{-1}(T_{ref}/T_0)$. Our model assumes a reference isotherm of $T_{ref}/T_0 = 0.46$ (thick gray line), or $T_{ref} = 600°C$ for $T_0 = 1300°C$; the corresponding plate isotherms are plotted as dashed lines. Depth axes for $L/V = 0.5$ Ma and 30 Ma (right side, in kilometers), calculated for an assumed diffusivity of $\kappa = 10^{-12}$ km^2/s, bound the plate ages spanned by the RTF data set.

[10] An important related concept is the fractional seismic coupling, defined as the ratio of the observed seismic moment release to the moment release expected from a plate tectonic model [*Scholz*, 2002]:

$$\chi = \frac{\Sigma M_{obs}}{\Sigma M_{ref}}. \tag{2}$$

Previous authors have made different assumptions in calculating the denominator of equation (2). In our study, we specified ΣM_{ref} in terms of a "thermal area of contact," A_T, which we obtained from a standard algorithm: the thermal structure of an RTF is approximated by averaging the temperatures of the bounding plates computed from a two-dimensional half-space cooling model [e.g., *Engeln et al.*, 1986; *Stoddard*, 1992; *Okal and Langenhorst*, 2000; *Abercrombie and Ekström*, 2001]. The isotherms and particular parameters of the algorithm are given in Figure 1. A_T is just the area of a vertical fault bounded from below by a chosen isotherm, T_{ref}, and its scaling relation is $A_T \propto L^{3/2}V^{-1/2}$. We define the average "thermal thickness" for this reference isotherm by $W_T \equiv A_T/L$. The cumulative moment release is $\Sigma M_{ref} = \mu L W_T V \Delta t_{cat}$, so equations (1) and (2) imply that χ is simply the ratio of W_E to W_T.

[11] The seismic coupling coefficient has the most direct interpretation if the reference isotherm T_{ref} corresponds to the brittle-plastic transition defined by the maximum depth of earthquake rupture [*Scholz*, 2002]. In this case, the value $\chi = 1$ quantifies the notion of "full seismic coupling" used in section 1. The focal depths of oceanic earthquakes do appear to be bounded by an isotherm, although estimates range from 400°C to 900°C [*Wiens and Stein*, 1983; *Trehu and Solomon*, 1983; *Engeln et al.*, 1986; *Bergman and Solomon*, 1988; *Stein and Pelayo*, 1991]. Ocean bottom seismometer (OBS) deployments [*Wilcock et al.*, 1990] and teleseismic studies using waveform modeling and slip inversions [*Abercrombie and Ekström*, 2001] tend to favor temperatures near 600°C. We therefore adopt this value as our reference isotherm. Actually, what matters for seismic coupling is not the absolute temperature, but its ratio to the mantle potential temperature T_0. We choose $T_{ref}/T_0 = 0.46$, so that a reference isotherm of 600°C implies $T_0 = 1300°C$, a typical value supported by petrological models of mid-ocean spreading centers [e.g., *Bowan and White*, 1994].

[12] Previous studies have shown that the χ values for RTFs are generally low. Referenced to the 600°C isotherm, most yield global averages of 10–30%, but again there is a lot of variability from one RTF to another. High values ($\chi > 0.8$) have been reported for many transform faults in the Atlantic Ocean [*Kanamori and Stewart*, 1976; *Muller*, 1983; *Wilcock et al.*, 1990], whereas low values ($\chi < 0.2$) are observed for Eltanin and other transform faults in the Pacific [*Kawaski et al.*, 1985; *Okal and Langenhorst*, 2000]. The consensus is for a general decrease in χ with spreading rate [*Kawaski et al.*, 1985; *Sobolev and Rundquist*, 1999; *Bird et al.*, 2002; *Rundquist and Sobolev*, 2002].

[13] By definition, low values of χ imply low values of the effective coupling width, W_E. However, is the actual RTF coupling depth that shallow? Several of the pioneering studies suggested this possibility [*Brune*, 1968; *Davies and Brune*, 1971; *Burr and Solomon*, 1978; *Solomon and Burr*, 1979]. From *Sleep*'s [1975] thermal model, *Burr and Solomon* [1978] obtained an average coupling depth corresponding to the 150°C isotherm (±100°C), and they supported their value with *Stesky et al.*'s [1974] early work on olivine deformation. Given the direct evidence of seismic rupture at depths below the 400°C isotherm, cited above, and experiments that show unstable sliding at temperatures of 600°C or greater [*Pinkston and Kirby*, 1982; *Boettcher et al.*, 2003], this "shallow isotherm" hypothesis no longer appears to be tenable [*Bird et al.*, 2002].

[14] However, the low values of χ could imply that RTFs have "thin, deep seismic zones," bounded from above by an isotherm in the range 400–500°C and from below by an isotherm near 600°C. Alternatively, the seismic coupling of RTFs may not depend solely on temperature; it might be dynamically maintained or depend on some type of lateral compositional variability. If so, does the low seismic coupling observed for RTFs represent a single-mode distribution of seismic and creeping patches, as in Appendix A, or does a particular patch sometimes slip seismically and sometimes aseismically?

[15] The low values of χ reflect the paucity of large earthquakes on RTFs, which can be characterized in terms of an upper cutoff magnitude. Like most other faulting environments, RTFs exhibit Gutenberg-Richter (GR) frequency-size statistics over a large range of magnitudes; that is, they obey a power law scaling of the form $\log N \propto -bm \propto -\beta \log M$, where N is the cumulative number above magnitude m and $\beta = (2/3)b$. The upper limit of the scaling region is specified by a magnitude cutoff m_C or an equivalent moment cutoff M_C, representing the "outer scale" of fault rupture. A variety of truncated GR distributions are available [*Molnar*, 1979; *Anderson and Luco*, 1983; *Main and Burton*, 1984; *Kagan*, 1991, 1993; *Kagan and Jackson*,

2000; *Kagan*, 2002a], but they all deliver a scaling relation of the form $\Sigma M \propto M_C^{1-\beta}$.

[16] The β values of individual transform faults are difficult to constrain owing to their remoteness and the correspondingly high detection thresholds of global catalogs. OBS deployments have yielded β values in the range 0.5–0.7 [*Trehu and Solomon*, 1983; *Lilwall and Kirk*, 1985; *Wilcock et al.*, 1990], while teleseismic studies of regional RTF seismicity have recovered values from 0.3 to 1.1 [*Francis*, 1968; *Muller*, 1983; *Dziak et al.*, 1991; *Okal and Langenhorst*, 2000]. The most recent global studies disagree on whether β is constant [*Bird et al.*, 2002] or depends on V [*Langenhorst and Okal*, 2002]. This observational issue is closely linked to theoretical assumptions about how RTF seismicity behaves at large magnitudes. *Bird et al.* [2002] adopted the truncated GR distribution of *Kagan and Jackson* [2000] (a three-parameter model); they showed that the Harvard CMT data set for the global distribution of RTFs is consistent with the self-similar value $\beta = 2/3$, and they expressed the seismicity variations among RTFs in terms of a cutoff moment M_C. They concluded that log M_C decreases quadratically with V. On the other hand, *Langenhorst and Okal* [2002] fit the data by allowing β to vary above and below an "elbow moment" that was also allowed to vary with V (a four-parameter model); they concluded that below the elbow, β increases linearly with V, while the elbow moment itself varies as approximately $V^{-3/2}$.

3. Seismicity Model

[17] We follow *Bird et al.* [2002] and adopt the three-parameter seismicity model of *Kagan and Jackson* [2000], in which an exponential taper modulates the cumulative GR distribution [see also *Kagan*, 2002a]:

$$N(M) = N_0 \left(\frac{M_0}{M}\right)^{\beta} \exp\left(\frac{M_0 - M}{M_C}\right). \tag{3}$$

M_0 is taken to be the threshold moment above which the catalog can be considered complete, and N_0 is the cumulative number of events above M_0 during the catalog interval Δt_{cat}. At low moment, N scales as $M^{-\beta}$, while above the outer scale M_C this cumulative number decays exponentially. We will refer to an event with moment M_C as an "upper cutoff earthquake"; larger events will occur, but with an exponentially decreasing probability. The total moment released during Δt_{cat} is obtained by integrating the product of M and the incremental distribution $n(M) = -dN/dM$,

$$\begin{aligned}\Sigma M &= \int_{M_0}^{\infty} M\, n(M) dM \\ &= N_0 M_0^{\beta} M_C^{1-\beta} \Gamma(1-\beta) e^{M_0/M_C}.\end{aligned}$$

Assuming $M_0 \ll M_C$, we obtain

$$\Sigma M \approx N_0 {M_0}^{\beta} {M_C}^{1-\beta} \Gamma(1-\beta). \tag{4}$$

For $\beta = 2/3$, the gamma function is $\Gamma(1/3) = 2.678\ldots$.

[18] Substituting equation (4) into equation (1) yields the formula for the effective seismic thickness W_E. In order to avoid equating small values of χ with shallow coupling depths, we multiply W_E by the total RTF length L to cast the analysis in terms of an effective seismic area A_E. We average over seismic cycles and equate an RTF moment rate with its long-catalog limit, $\dot{M} \equiv \lim_{\Delta t_{cat}\to\infty} \Sigma M/\Delta t_{cat}$. This reduces equation (1) to the expression

$$A_E = \dot{M}/(\mu V). \tag{5}$$

The effective area is thus the total seismic potency, M/μ, per unit slip, averaged over many earthquake cycles.

[19] Similarly, the outer scale of fault rupture can be expressed in terms of upper cutoff moment, $M_C = \mu A_C D_C$, where A_C is the rupture area and D_C is the average slip of the upper cutoff earthquake. In this notation, the long catalog limit of equation (4) can be written $\dot{M} = \dot{N}_0 M_0^{\beta} M_C^{1-\beta} \Gamma(1-\beta)$, where $\dot{N}_0$ is the average number of events with moment above M_0 per unit time. We employ a nondimensionalized version of this event rate parameter, which we call the seismic productivity:

$$\nu_0 = \frac{\dot{N}_0 M_0}{\mu A_T V}. \tag{6}$$

The seismic productivity is the cumulative event rate normalized by the rate of events of moment M_0 needed to attain full seismic coupling over the thermal area of contact A_T. For the RTFs used in this study, $M_C \gg M_0$, so that $\nu_0 \ll 1$. With these definitions, our model for the seismic coupling coefficient becomes

$$\chi = A_E/A_T = \nu_0 (M_C/M_0)^{1-\beta} \Gamma(1-\beta). \tag{7}$$

4. Data

[20] We delineated the RTFs using altimetric gravity maps [*Smith and Sandwell*, 1997], supplemented with T phase locations from the U.S. Navy Sound Surveillance System (SOSUS) of underwater hydrophones [*Dziak et al.*, 1996, 2000; R. P. Dziak, SOSUS locations for events on the western Blanco Transform Fault, personal communication, 1999]. Like other strike-slip faults, RTFs show many geometric complexities, including offsets of various dimensions (see section 1 for references), so that the definition of a particular fault requires the choice of a segmentation scale. Given the resolution of the altimetry and seismicity data, we chose offsets of 35 km or greater to define individual faults. Fault lengths L for 78 RTFs were calculated from their endpoint coordinates, and their tectonic slip rates were computed from the NUVEL-1 plate velocity model [*DeMets et al.*, 1990]. We winnowed the fault set by removing any RTF with $L < 75$ km and $A_T < A_T^{min} = 350$ km^2. This eliminated small transform faults with uncertain geometry or seismicity measures significantly contaminated by ridge crest normal faulting. The resulting fault set comprised 65 RTFs with a combined length of 16,410 km (Figure 2).

4.1. Seismicity Catalogs

[21] We compiled a master list of RTF seismicity by collating hypocenter and magnitude information from the

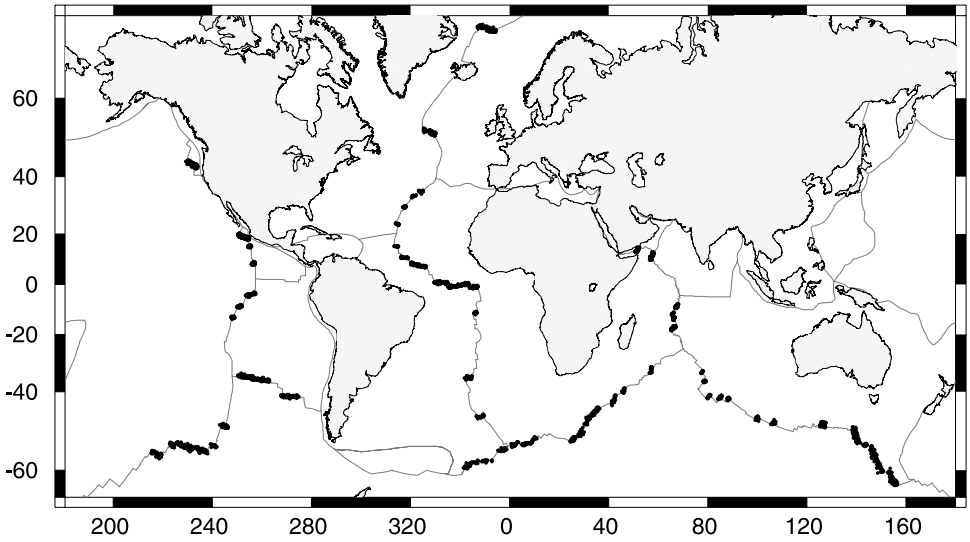

Figure 2. Global distribution of the 65 mid-ocean ridge transform faults (RTFs) used in this study. The faults were selected to have $L > 75$ km and $A_T > 350$ km^2 and have been delineated by plotting all associated earthquakes from the ISC m_S and Harvard CMT catalogs (black dots). The cumulative fault length is 16,410 km.

Harvard CMT and the International Seismological Center (ISC) online bulletin (1964–1999, available at http://www.isc.ac.uk) catalogs. We created an earthquake catalog for each RTF comprising all events with locations (ISC epicenters for 1964–1999, CMT epicentroids for 2000–2002) that fell within a region extending 80 km on either side of the fault or 50 km from either end. To avoid overlap in the cases where faults were close together, we reduced the radii of the semicircular regions capping the fault ends until each earthquake was associated with a unique RTF. The tectonic parameters and seismicity compilations for individual RTFs are summarized in Appendix B.

[22] Three types of magnitude data were included in our catalogs, body wave (m_b) and surface wave (m_S) magnitudes from the ISC (1964–1999) and moment magnitude (m_W) from the Harvard CMT (1976–2002). Using the moment tensors from the latter data set, we further winnowed the catalog of events whose null axis plunges were less than 45° in order to eliminate normal-faulting earthquakes. Normal-faulting events without CMT solutions could not be culled from the m_b and m_S data sets, although their contributions to the total moment are probably small. The three magnitude distributions for the 65 RTFs indicate average global network detection thresholds at $m_b = 4.7$, $m_S = 5.0$, and $m_W = 5.4$, with slightly higher thresholds for m_b and m_W in the Southern Ocean, at 4.8 and 5.6, respectively. We use the higher threshold values in our analysis to avoid any geographic bias.

[23] The location uncertainties for RTF events depend on geographic position, but for events larger than the m_S threshold of 5.0, the seismicity scatter perpendicular to the fault traces has an average standard deviation of about 25 km. The spatial window for constructing the fault catalogs was chosen to be sufficiently wide to comprise essentially all of the CMT events with appropriately oriented strike-slip mechanisms. Increasing the window dimensions by 20% only increased the total number of events with $m_W > 5.6$ from 548 to 553 (+0.9%) and their cumulative CMT strike-slip moment from 1.205×10^{21} N m to 1.212×10^{21} N m (+0.6%).

[24] A potentially more significant problem was the inclusion of seismicity near the RTF end points, where the transition from spreading to transform faulting is associated with tectonic complexities [*Behn et al.*, 2002]. However, completely eliminating the semicircular window around the fault ends only decreased the event count to 517 (−5.7%) and the cumulative moment to 1.162×10^{21} N m (−3.6%), which would not change the results of our scaling analysis.

[25] Some large earthquakes with epicenters near ridge-transform junctures actually occur on intraplate fracture zones, rather than the active RTF. Including these in the RTF catalogs can bias estimates of the upper cutoff magnitude, m_C. A recent example is the large ($m_W = 7.6$) earthquake of 15 July 2003 east of the Central Indian Ridge, which initiated near the end of a small (60 km long) RTF and propagated northeastward away from the ridge-transform junction [*Bohnenstiehl et al.*, 2004]. A diagnostic feature of this type of intraplate event is a richer aftershock sequence, distinct from the depleted aftershock sequences typical of RTFs (see section 4.3). An example that occurred during the time interval of our catalog, the $m_W = 7.2$ event of 26 August 1977, was located on the fracture zone 130 km west of the Bullard (A) RTF fracture zone. This event and its three aftershocks ($m_b \geq 4.8$) were excluded from our data set by our windowing algorithm. We speculate that the anomalously large ($m \approx 8$) earthquake of 10 November 1942, located near the end of the Andrew Bain RTF in the southwest Indian Ocean [*Okal and Stein*, 1987] was a fracture zone event, rather than an RTF earthquake as assumed in some previous studies [e.g., *Langenhorst and Okal*, 2002; *Bird et al.*, 2002].

4.2. Calibration of Surface Wave Magnitude

[26] The calibration of surface wave magnitude m_S to seismic moment M for oceanic environments has been discussed by *Burr and Solomon* [1978], *Kawaski et al.*

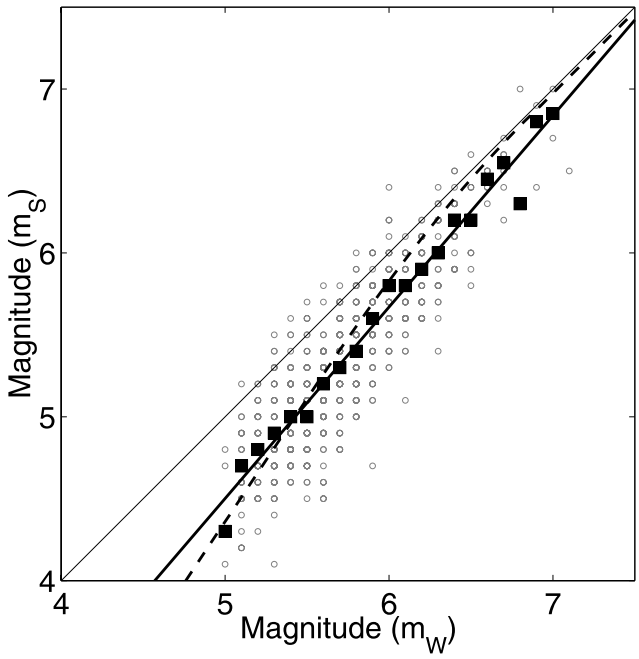

Figure 3. Calibration of ISC surface wave magnitudes to Harvard moment magnitudes. Magnitudes sampled by the data are shown as small circles. The regression line, $m_S = 1.17\ m_W - 1.34$ (thick solid line), provides a better fit to the median values of m_S (solid squares) than the nonlinear relation of *Ekström and Dziewonski* [1988] (dashed line).

[1985], and *Ekström and Dziewonski* [1988]. Ekström and Dziewonski derive an empirical relationship to calibrate ISC surface wave magnitudes to CMT moments, and they list the various factors to explain why regional subsets might deviate from a global average. On a m_S–m_W plot (Figure 3), the medians for our data agree with their global curve at low magnitudes but fall somewhat below for $m_W \geq 6$. Overall, the data are better matched by a linear fit to the medians: $m_S = 1.17\ m_W - 1.34$. We used this linear relationship to convert the ISC values of m_S to seismic moment.

[27] With this calibration, the total moment release rates for all RTFs in our data set are 4.39×10^{19} N m/yr for the 36-year m_S catalog and 4.72×10^{19} N m/yr for the 25.5-year m_W catalog. The 10% difference, as well as the scatter in the ratio of the two cumulative moments for individual RTFs, is consistent with the fluctuations expected from observational errors and the Poisson (time-independent) model of seismicity employed in our statistical treatment. The Poisson model ignores any clustering associated with foreshock-main shock-aftershock sequences, which are known to introduce bias in the analysis of continental seismicity [e.g., *Aki*, 1956; *Knopoff*, 1964; *Gardner and Knopoff*, 1974].

4.3. Aftershock Productivity

[28] RTF earthquakes generate very few aftershocks, however. Defining an aftershock as an event of lower magnitude that occurred within 30 days and 100 km of a main shock, we counted aftershocks above a magnitude threshold m_0. Figure 4 compares the average count per main shock with similar data for strike-slip earthquakes in southern California [*Kisslinger and Jones*, 1991] and Japan [*Yamanaka and Shimazaki*, 1990]. The data can be described by an aftershock law of the form

$$\log N_{\text{after}} = \alpha(m_{\text{main}} - m_0 - \Delta m_{\text{after}}). \tag{8}$$

The triggering exponent α is a fundamental scaling parameter of the Epidemic Type Aftershock Sequence (ETAS) model [*Kagan and Knopoff*, 1991; *Ogata*, 1988; *Guo and Ogata*, 1997; *Helmstetter and Sornette*, 2002]; the offset Δm_{after} is related to the magnitude decrement of the largest probable aftershock, given by Båth's law to be about 1.2 [*Felzer et al.*, 2002; *Helmstetter and Sornette*, 2003a]. The continental data in Figure 4 yield $\alpha \approx 0.8$, which agrees with previous studies [*Utsu*, 1969; *Yamanaka and Shimazaki*, 1990; *Guo and Ogata*, 1997; *Helmstetter and Sornette*, 2003a], and $\Delta m_{\text{after}} \approx 0.9$, consistent with the data for southern California [*Felzer et al.*, 2002; *Helmstetter*, 2003].

[29] In the case of RTFs, the aftershock productivity is so low that the data for the smallest main shock magnitudes approach background seismicity (Figure 4). RTF earthquakes are consistent with $\alpha = 0.8$ and yield $\Delta m_{\text{after}} \approx 2.2$, much larger than the continental value. In other words, the key parameter of the ETAS model, the "branching ratio" $n = 10^{-\alpha \Delta m_{\text{after}}} b/(b - \alpha)$, which is the average over all main shock magnitudes of the mean number of events triggered by a main shock [*Helmstetter and Sornette*, 2002], is more than an order of magnitude less for RTF seismicity than the critical value of unity approached by continental strike-slip faulting. If the ETAS model holds for RTF seismicity, then the low branching ratio ($n \approx 0.1$) implies that most (~90%) RTF earthquakes are driven by tectonic loading and subseismic slip, rather than triggered by other seismic events [*Helmstetter and Sornette*, 2003b]. This observation underlines a central difference between RTF seismicity and the SAF model.

5. Scaling Analysis

[30] The RTFs are arrayed according to their fault lengths L and slip velocities V in Figure 5. The data set spans about an order of magnitude in each of these tectonic variables. The seismicity of an individual RTF is represented by its "cumulative moment magnitude," obtained by plugging ΣM from the Harvard CMT catalog into *Kanamori*'s [1977] definition of moment magnitude:

$$m_\Sigma = \frac{2}{3}(\log \Sigma M - 9.1). \tag{9}$$

There were only 11 RTFs with $m_\Sigma \geq 7.0$; five were in the central Atlantic, including the Romanche transform fault, which had the largest CMT moment release ($m_\Sigma = 7.46$). The catalogs were too short to allow a robust estimation for individual faults with lower seismicity levels; therefore we grouped the data into bins spanning increments of the geologic control variables, L, V, and A_T. For each control variable, we adjusted the boundaries of the bins so that the subsets sampled the same numbers of events, more or less, and were numerous enough to estimate the seismicity parameters. After some experimentation, we settled on four subsets, each containing an average of about 130 and

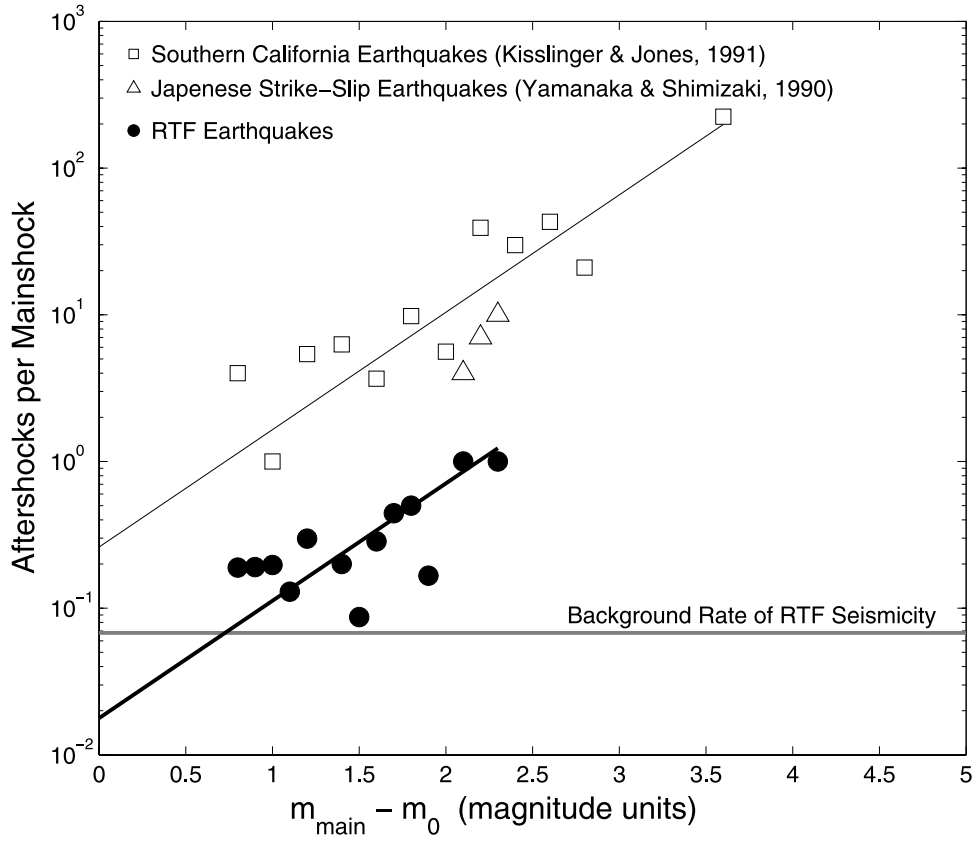

Figure 4. Average number of aftershocks above a magnitude threshold m_0 for each main shock plotted against $m_{\text{main}} - m_0$ for earthquakes on RTFs (solid symbols) and continental strike-slip faults (open symbols). RTF aftershocks were defined as events with an ISC m_b greater than or equal to $m_0 = 4.8$ that occurred within 30 days and 100 km of a main shock. The continental data sets were complied by *Kisslinger and Jones* [1991] and *Yamanaka and Shimazaki* [1990] using local magnitude thresholds of $m_0 = 4.0$ and 4.5, respectively. Both continental and RTF aftershocks are consistent with a slope $\alpha = 0.8$ (inclined lines), but the latter are about 1.3 orders of magnitude less frequent than the former. Note that at low main shock magnitudes, RTF aftershock rates approach background seismicity (horizontal line).

190 earthquakes for the m_W and m_S catalogs, respectively. The boundaries of the subsets are indicated in Figure 5.

5.1. Seismicity Parameters

[31] We estimated the seismicity parameters by fitting equation (3) to the data subsets using a maximum likelihood method. Event frequencies were binned in 0.1 increments of log M for the Harvard CMT data and 0.1 increments of m_S for the ISC data. The random variable representing the observed number of earthquakes, n_k, in each bin of moment width ΔM_k was assumed to be Poisson distributed with an expected value, $\bar{n}_k \approx -\Delta M_k dN(M_k)/dM$, where the cumulative distribution $N(M)$ was specified by equation (3). This yielded the likelihood function:

$$\text{Lik}(\beta, M_C) = \sum_k \left\{ \ln\left[n_k N_0 \left(\frac{\beta}{M_k} + \frac{1}{M_C} \right) \left[\frac{M_k}{M_0} \right]^{-\beta} \cdot \exp\left[\frac{M_0 - M_k}{M_C} \right] \right] - N_0 \left(\frac{\beta}{M_k} + \frac{1}{M_C} \right) \left[\frac{M_k}{M_0} \right]^{-\beta} \cdot \exp\left[\frac{M_0 - M_k}{M_C} \right] - \ln(n_k!) \right\}. \quad (10)$$

Our procedure followed *Smith and Jordan*'s [1988] analysis of seamount statistics, but it differed from most treatments of earthquake frequency-size data [e.g., *Aki*, 1965; *Bender*, 1983; *Ogata*, 1983; *Frohlich and Davis*, 1993; *Kagan and Jackson*, 2000; *Wiemer and Wyss*, 2000], which take the GR distribution or its truncated modification as the underlying probability function (compare equation (10) with equation (12) of *Kagan and Jackson* [2000]).

[32] The method is illustrated in Figure 6, where it has been applied to the m_W and m_S catalogs collated for all RTFs used in this study. On the basis of the seismicity roll-off at low magnitudes, we fixed the threshold magnitudes at 5.6 for m_W and 5.5 for recalibrated m_S. The maximum likelihood estimator for N_0 is the cumulative number of events observed above the corresponding threshold moments M_0 (531 and 750, respectively). Figures 6c and 6d contour the likelihood functions for the other two parameters, the power law exponent β and upper cutoff moment M_C. The two catalogs give very similar estimates: $\beta = 0.72$, $M_C = 1.42 \times 10^{19}$ N m ($m_C = 6.70$) for the Harvard CMT catalog, and $\beta = 0.70$, $M_C = 1.58 \times 10^{19}$ N m ($m_C = 6.73$) for the recalibrated ISC catalog. The 95% confidence region for each estimate includes the other estimate, as well as the maximum likelihood estimate obtained by fixing β at the self-similar value of 2/3. Our results thus agree with those of *Bird et al.* [2002], who found RTF seismicity to be consistent with

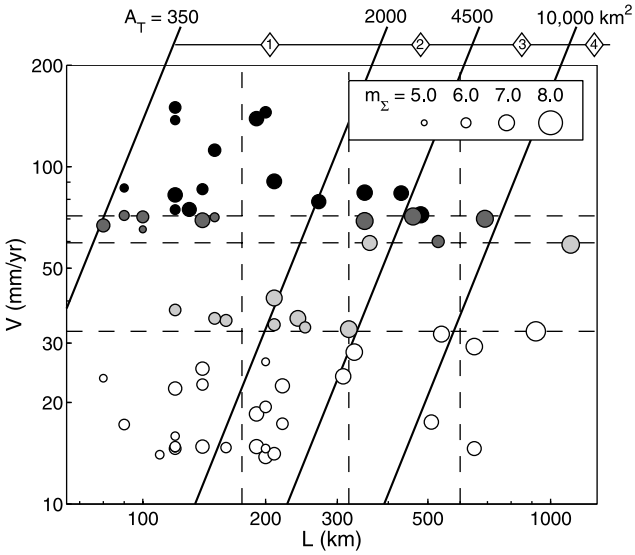

Figure 5. Distribution of fault lengths L and slip rates V for the 65 RTFs used in this study (circles). The symbols have been sized according to the cumulative moment magnitude m_Σ, defined by equation (9), and shaded based on the four slip rate bins separated by horizontal dashed lines. Values separating the fault length bins (vertical dashed lines) and the thermal area bins (inclined solid lines) used in our scaling analysis are also shown.

self-similar scaling below the upper cutoff moment. The self-similar assumption yields conditional values of M_C that differ by only 1% between the two catalogs (diamonds in Figure 6).

[33] The truncated GR model provides an adequate fit to the global RTF data sets. It slightly underestimates the frequency of the largest earthquakes, predicting only one event of magnitude 7 or larger compared to the three observed in both catalogs; however, the discrepancy is not statistically significant even at a low (74%) confidence level. The Harvard CMT catalog also shows a modest depletion of events just below M_C, but this feature is not evident in the ISC data.

[34] Maximum likelihood estimates of total seismic moment ΣM, upper cutoff moment M_C, and seismic productivity ν_0 derived from binned data allow us to investigate how these parameters are distributed with fault length L and slip velocity V (see Appendix C for figures and additional details). Because the catalogs are relatively short, the scatter in the individual fault data is large, especially for the smaller faults. Some variation may also be due to recent changes in plate motion, which may affect the geometry and possibly the thermal structure of an RTF. The maximum likelihood estimates, which correctly average over the Poissonian variability of the catalogs, are more systematic. ΣM and M_C increase with L, whereas ν_0 decreases. The correlations in V suggest weak positive trends in ΣM and ν_0 and a weak negative trend in M_C. A proper interpretation of these correlations must account for any correlation between the two tectonic variables.

[35] According to the thermal scaling hypothesis, the seismicity parameters should depend on fault length and slip rate through the thermal area of contact, A_T (Figure 1). We sorted the data into the A_T bins shown in Figure 5 and estimated the seismicity parameters for the four subgroups. Figures 7 and 8 show the results for the Harvard CMT catalog. The estimates for $\beta = 2/3$ (numbered diamonds) fall within the 50% confidence regions for the unconstrained estimates (shaded areas) in all four bins (Figure 8a), again consistent with self-similar scaling below the cutoff moment. There is more scatter in the A_T binned estimates from the ISC catalog, but self-similar scaling is still acceptable at the 95% confidence level. We therefore fixed β at 2/3 and normalized the seismicity models for the four A_T groups according to equation (6). The seismicity models obtained from both catalogs indicate that as A_T increases, the upper cutoff moment M_C increases and the seismic productivity ν_0 decreases, while the area under the curve stays about the same (e.g., Figure 8b). These statements can be quantified in terms of scaling relations involving the three areal measures A_T, A_E, and A_C.

5.2. Seismic Coupling

[36] We computed the effective seismic area $A_E = LW_E$ from equation (1) assuming the shear modulus, $\mu = 44.1$ GPa, which is the lower crustal value from the Preliminary Reference Earth Model (PREM) [*Dziewonski and Anderson*, 1981]. On plots of A_E versus A_T (Figure 9),

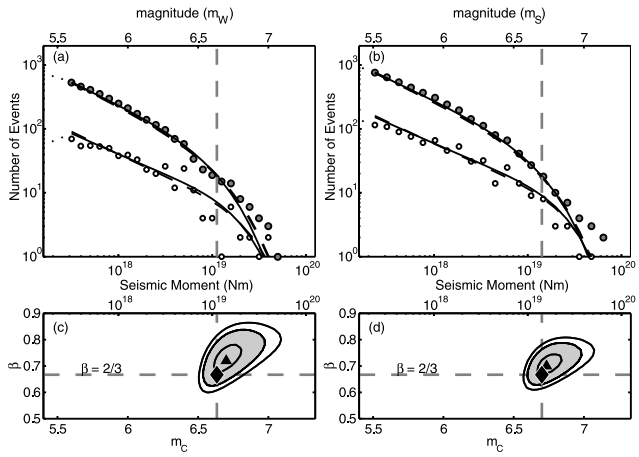

Figure 6. Global frequency-moment distributions for RTF earthquakes from (a) the Harvard CMT catalog and (b) recalibrated ISC catalog, with corresponding log likelihood maps (Figures 6c and 6d) for the model parameters. Numbers of events in discrete m_W bins (open circles) and cumulative numbers of events (solid circles) are fit with a three-parameter tapered GR distribution (dashed lines) and a tapered GR distribution with a low-moment slope fixed at $\beta = 2/3$ (solid lines). In both cases the upper cutoff moment M_C is taken at the best fit value. Triangles are the maximum likelihood solutions; contours show the 99%, 95%, and 50% confidence regions. For both catalogs, the solutions constrained by $\beta = 2/3$ (diamonds) lie within the 95% confidence contours of the unconstrained solution (shaded regions), and m_C for the two solutions are within a tenth of a magnitude unit. The threshold moment magnitude m_0 was set at 5.6 for CMT data and 5.5 for recalibrated ISC data.

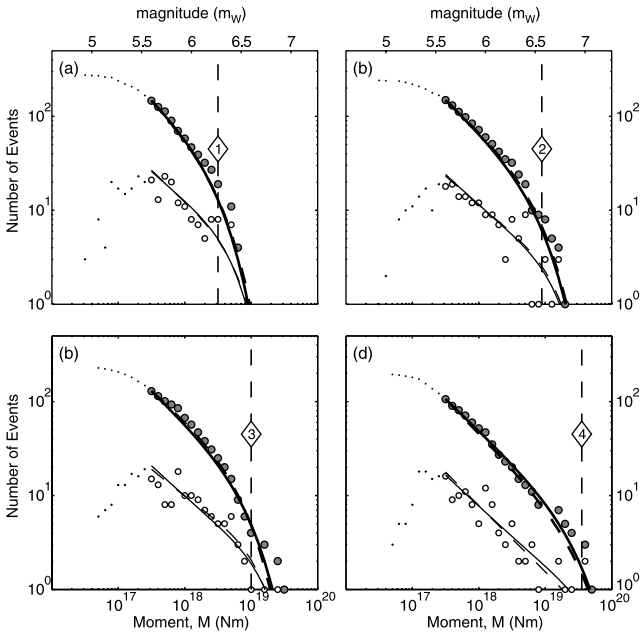

Figure 7. Frequency-moment distributions derived from the Harvard CMT catalog by binning RTFs according to the A_T divisions shown at the top of Figure 5: (a) 350–2000 km^2, (b) 2000–4500 km^2, (c) 4500–10,000 km^2, and (d) >10,000 km^2. Numbers of events in discrete m_W bins (open circles) and cumulative numbers of events (solid circles) are fit by maximum likelihood procedure with a three-parameter tapered GR distribution (dashed lines) and a tapered GR distribution with a low-moment slope fixed at $\beta = 2/3$ (solid lines). Dots show data below the threshold moment magnitude of $m_0 = 5.6$. Vertical dashed lines are the maximum likelihood estimates of M_C for $\beta = 2/3$.

the data for individual small faults scatter by as much as 2 orders of magnitude, but the maximum likelihood values for the binned data form linear arrays consistent with a constant coupling coefficient. To test the constant χ hypothesis, we constructed the likelihood function for the parameters of a more general scaling law,

$$A_E/A_E^* = (A_T/A_T^*)^{\psi}, \tag{11}$$

where A_E^* and A_T^* are reference values. The maximum likelihood estimates of the scaling exponent are $\psi = 1.03^{+0.20}_{-0.14}$ for the m_W data and $\psi = 0.87^{+0.17}_{-0.11}$ for the m_S data (here and elsewhere the uncertainties delineate the 95% confidence regions). Both data sets are consistent with $\psi = 1$; moreover, with the exponent fixed at unity, both give the same value of the coupling coefficient, $\chi = A_E^*/A_T^* = 0.15^{+0.02}_{-0.02}$ and $0.15^{+0.03}_{-0.01}$, respectively.

[37] Therefore our results support the simplest version of the thermal scaling hypothesis: the long-term cumulative moment release depends on the tectonic parameters L and V only through the thermal relation $A_E \propto A_T \propto L^{3/2}V^{-1/2}$. The constant χ model agrees well with the data (Figure C1), except at large V, where the data fall below the model. This discrepancy is due in part to the weak negative correlation between L and V, evident in Figure 5. As a check, we compensated the values of ΣM for thermal scaling and replotted them against L and V; the maximum likelihood estimates for the rebinned data showed no significant residual trends.

5.3. Upper Cutoff Earthquake

[38] To calculate the rupture area $A_C = L_C W_C$ of the upper cutoff earthquake from its seismic moment $M_C = \mu A_C D_C$, some assumption must be made about how the average slip D_C scales with the rupture length L_C and width W_C. Given the continuing controversy over the slip scaling for large strike-slip earthquakes (see introduction), we considered a scaling relation of form

$$D_C = \frac{\Delta\sigma}{\mu} L_C^{\lambda} W_C^{1-\lambda}, \tag{12}$$

where $0 \le \lambda \le 1$ and $\Delta\sigma$ is the static stress drop, which we took to be independent of earthquake size. The various

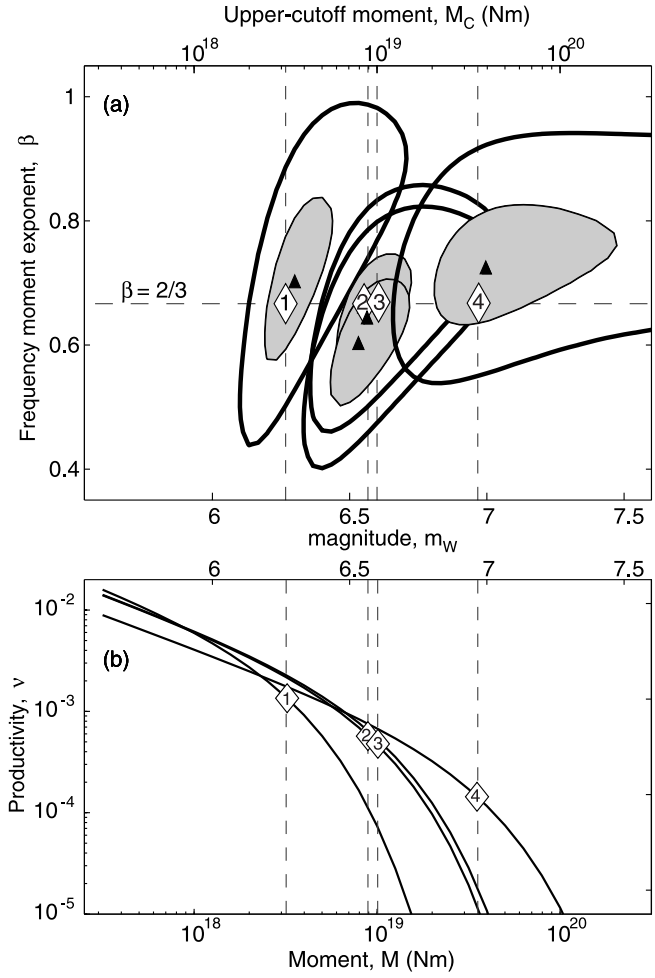

Figure 8. (a) Parameter estimates and (b) frequency-moment distributions derived from the A_T-binned data of Figure 7. Log likelihood maps in Figure 8a show the upper cutoff moment M_C and low-moment slope β corresponding to the four A_T bins. Triangles are the maximum likelihood solutions; contours show the 95% and 50% confidence regions. The solutions constrained by $\beta = 2/3$ (diamonds) lie within the 50% confidence contours of the unconstrained solution (shaded regions), and m_C for the two solutions are within a tenth of a magnitude unit.

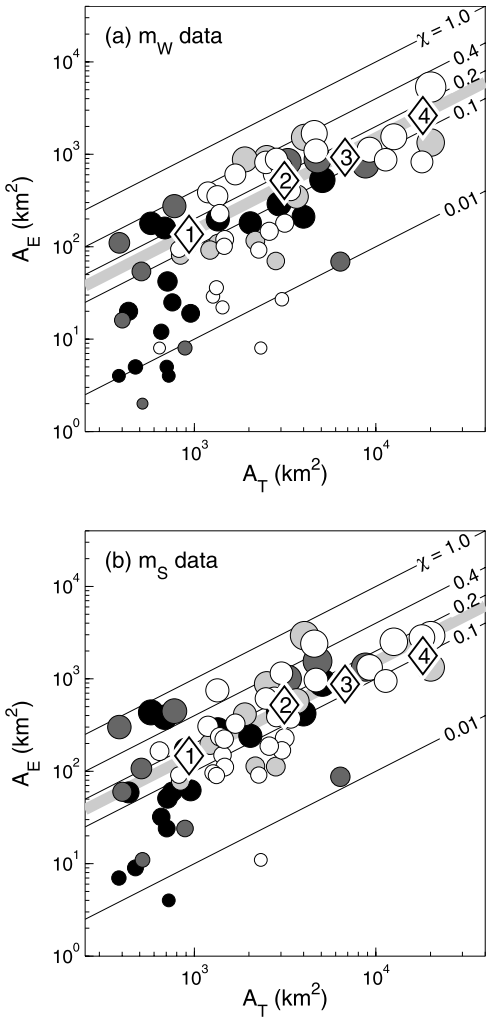

Figure 9. Effective seismic area A_E versus thermal area of contact A_T for (a) the Harvard CMT catalog and (b) recalibrated ISC m_S catalog. Symbols show data for individual RTFs (circles) and maximum likelihood estimates from the A_T-binned data for $\beta = 2/3$ (numbered diamonds). The data bins, as well as the circle sizes and shading, are given in Figure 5; fits are shown in Figures 7 and 8. The abscissa values for the diamonds are the averages of A_T in each bin weighted by the plate tectonic moment release rate $\mu A_T V$. Thin lines correspond to the seismic coupling factors χ for $T_{ref} = 600°C$. The maximum likelihood values are consistent with a simple linear scaling $A_E \sim A_T$ (Table 1) and $\chi = 0.15$ (thick gray line).

models extant in the literature correspond to different values of the scaling exponent λ. The *W* model preferred by *Romanowicz* [1992, 1994] and *Romanowicz and Ruff* [2002] is given by $\lambda = 0$, whereas the *L* model preferred by *Scholz* [1982], *Shimazaki* [1986], *Scholz* [1994a, 1994b], *Pegler and Das* [1996], *Wang and Ou* [1998], *Shaw and Scholz* [2001], and *Hanks and Bakun* [2002] corresponds to $\lambda = 1$. The intermediate value, $\lambda = 1/2$, specifies the self-similar slip scaling advocated for large continental strike-slip earthquakes by *Bodin and Brune* [1996], *Mai and Beroza* [2000], and P. Somerville (personal communication, 2003), here called the *S* model. As noted in Appendix A, the best data for continental regions, including the large strike-slip events in Izmit, Turkey (1999), and Denali, Alaska (2002), tend to favor the *S* model (P. Somerville, personal communication, 2003). *Langenhorst and Okal* [2002] adopted the *W* model for their analysis of RTF seismicity; however, for large RTF earthquakes, no independent observations of fault slip and rupture dimensions are available to constrain λ.

[39] On the basis of the rupture depth observations cited previously and the success of thermal scaling in explaining the ΣM data, we assumed the vertical extent of faulting during large earthquakes scales with the average thermal thickness $W_T \equiv A_T/L$,

$$W_C = \eta W_T. \tag{13}$$

Here η is a constant whose value is unimportant to the scaling analysis but presumably lies between χ (thin seismic zone) and unity (thick seismic zone). From equation (12), the upper cutoff area can then be expressed as

$$A_C = (M_C/\Delta\sigma)^{\frac{1}{\lambda+1}}(\eta W_T)^{\frac{2\lambda-1}{\lambda+1}}. \tag{14}$$

[40] Figure 10 displays the data on plots of A_C versus A_T for $\lambda = 1/2$ (*S* model) assuming a constant stress drop of $\Delta\hat{\sigma} = 3$ MPa. The maximum likelihood estimates for the four A_T bins again form linear arrays, but the slopes are significantly less than unity. We fit the data with the scaling relation

$$A_C/A_C^* = (A_T/A_T^*)^{\gamma} \tag{15}$$

and obtained maximum likelihood estimates and 95% confidence regions for the upper cutoff scaling exponent $\gamma = 0.54^{+0.29}_{-0.32}$ for the m_W catalog and $\gamma = 0.54^{+.33}_{-.34}$ for the m_S catalog. Varying the slip-scaling exponent λ gave values of γ that ranged from 0.30 to 0.61, depending on the data set (Figure 11). In all cases, the data are consistent with $\gamma = 1/2$, which we adopted as our model value for upper cutoff scaling.

[41] Under the constraints of our model (e.g., constant $\Delta\sigma$, γ), the seismicity data can, in principle, determine the slip-scaling exponent λ. Combining the conductive cooling equation with equations (14) and (15) yields a general relation between the upper cutoff moment and the RTF tectonic parameters: $M_C \propto L^{(\lambda+1)\{3\gamma/2\}-\lambda+1/2}V^{-(\lambda+1)\{\gamma/2\}+\lambda-1/2}$. For $\gamma = 1/2$ we find

$$\begin{aligned} &W \text{ model} && M_C \propto L^{5/4}V^{-3/4}, \\ &S \text{ model} && M_C \propto L^{9/8}V^{-3/8}, \\ &L \text{ model} && M_C \propto L. \end{aligned} \tag{16}$$

The *L* model thus implies that the cutoff moment M_C is proportional to the tectonic fault length and independent of

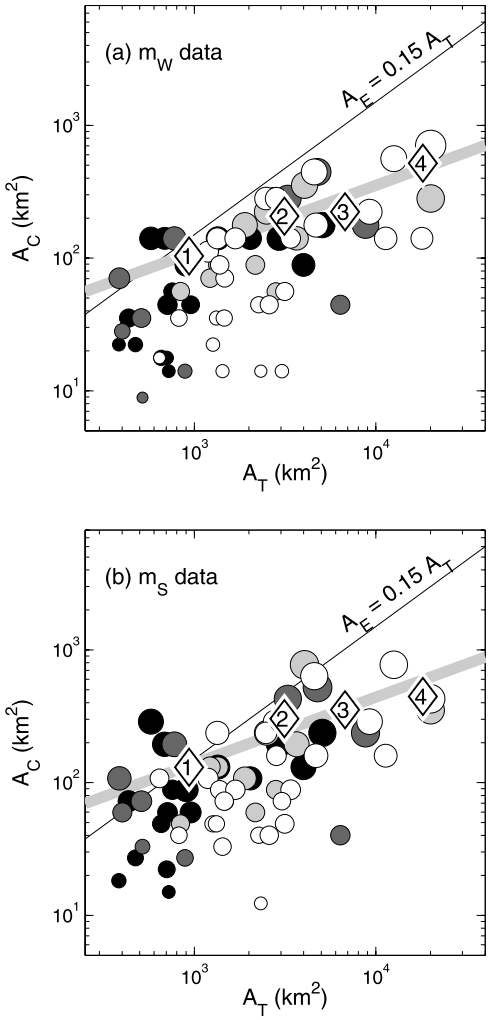

Figure 10. Upper cutoff area A_C versus thermal area of contact A_T for (a) the Harvard CMT catalog and (b) recalibrated ISC m_S catalog. Symbols show largest earthquakes for individual RTFs (circles) and maximum likelihood estimates from the A_T-binned data for $\beta = 2/3$ (numbered diamonds). The data bins, as well as the circle sizes and shading, are given in Figure 5; fits are shown in Figures 7 and 8. Calculations assume $A_C = (M_C/\Delta\sigma)^{2/3}$, corresponding to the *S* model of slip scaling ($\lambda = 1/2$), and a constant stress drop of $\Delta\sigma = 3$ MPa. The abscissa values for the diamonds are the averages of A_T in each bin weighted by the plate tectonic moment release rate $\mu A_T V$. The maximum likelihood values are consistent with the scaling relation $A_C \sim A_T^{1/2}$ (Table 1); the best fit (thick gray line) crosses the scaling relation for effective seismic area (thin black line) at $\hat{A}_T^* = 555$ km^2 (Figure 10a) and $\hat{A}_T^* = 862$ km^2 (Figure 10b).

the tectonic slip rate. Decreasing λ introduces a negative dependence on V, while maintaining an approximate proportionality between M_C and L.

[42] The L-binned estimates of M_C (Figures C2a and C2c) do show near proportionality, although they cannot resolve the small differences among the models in equation (16). The negative trends in the V-binned estimates of M_C, seen in both the m_W and m_S data sets (Figure C2b and C2d), are more diagnostic, favoring $\lambda < 1$. After compensating for the scalings $\lambda = 1/2$ and $\gamma = 1/2$, we found that the residual correlations of M_C in L and V were negligible, so we adopted the *S* model for our subsequent calculations. However, given the uncertainties and restrictive modeling assumptions, neither the L nor W end-member models can be firmly rejected with the data in hand.

5.4. Seismic Productivity

[43] The parameter in the truncated GR distribution most accurately estimated by the seismicity data is N_0, the total number of events above the moment threshold M_0. Its value depends primarily on the more numerous smaller earthquakes and is therefore insensitive to the upper cutoff behavior. Its normalized version, the seismic productivity ν_0, can be related to the other seismicity parameters through equation (7):

$$\nu_0 = \chi\ (M_0/M_C)^{1-\beta}/\Gamma(1-\beta). \tag{17}$$

The right-hand side of equation (17) can be evaluated directly from the scaling relations we have already derived: $\nu_0 \propto A_T^{-\gamma(\lambda+1)(1-\beta)+\psi-1}$. The preferred exponents ($\psi = 1$, $\beta = 2/3$, $\gamma = 1/2$, $\lambda = 1/2$) in our scaling model given in equations (3), (11), (12), and (15) therefore imply

$$\nu_0 \propto A_T^{-1/4} \propto L^{-3/8} V^{1/8}. \tag{18}$$

Because the form of this scaling relation has been determined primarily from the frequency of large earthquakes, the data on ν_0 provide an independent test of the model.

[44] Figure 12 plots the ν_0 observations against A_T. Unlike the other seismicity parameters, the scaling of ν_0 is insensitive to the magnitude moment calibration. We can therefore use the uncalibrated m_b catalog, as well as the m_W and calibrated m_S catalogs, in evaluating the model. All three data sets show a decrease in ν_0 very close to the model-predicted trend of $A_T^{-1/4}$ (gray lines). The data in

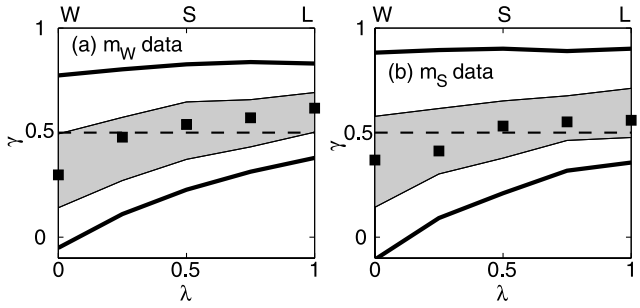

Figure 11. Maximum likelihood estimates (solid squares) of the characteristic area scaling exponent γ conditional on the slip-scaling exponent λ, obtained from (a) the Harvard CMT catalog and (b) recalibrated ISC m_S catalog. The best estimates for both catalogs cross the model value $\gamma = 1/2$ (dashed line) near $\lambda = 1/2$, which is our preferred exponent for slip scaling (*S* model). The end-member *W* and *L* models of slip scaling are also consistent with $\gamma = 1/2$ at the 50% confidence level (shaded band). Thick lines delineate 95% confidence region for the conditional estimate.

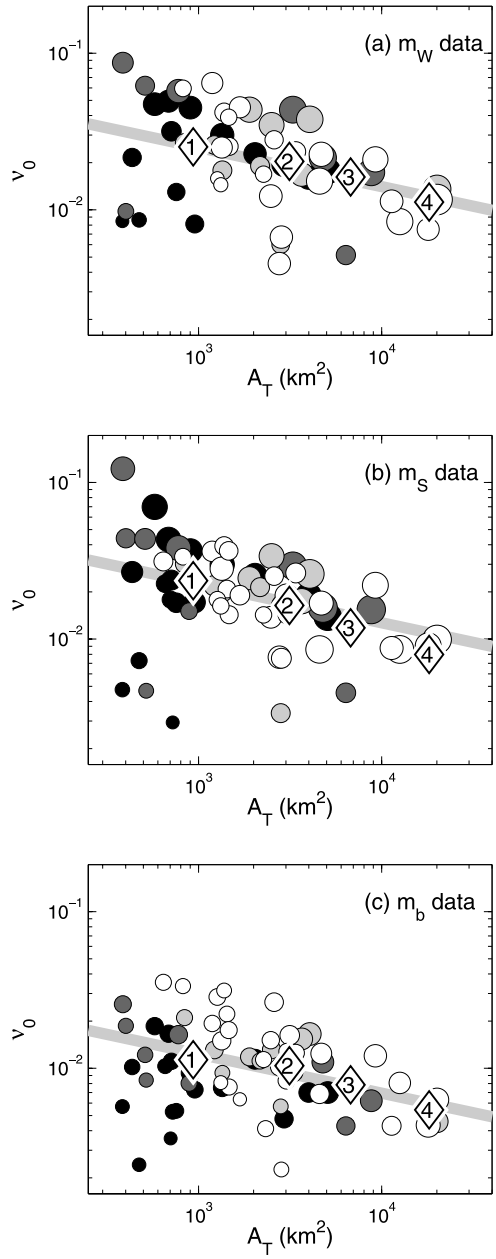

Figure 12. Seismic productivity ν_0 versus thermal area of contact A_T for (a) the Harvard CMT catalog, (b) recalibrated ISC m_S catalog, and (c) ISC m_b catalog. Symbols show normalized event counts for individual RTFs (circles) and maximum likelihood estimates from the A_T-binned data for $\beta = 2/3$ (numbered diamonds). The data bins, as well as the circle sizes and shading, are given in Figure 5; fits are shown in Figures 7 and 8. The magnitude threshold for the ISC m_b catalog was set at 4.8, providing significantly more events (2278) than either the Harvard CMT catalog (548) or the recalibrated ISC m_S catalog (890). The abscissa values for the diamonds are the averages of A_T in each bin weighted by the plate tectonic moment release rate $\mu A_T V$. The data are consistent with $\nu_0 \sim A_T^{-1/4}$ (thick gray lines), providing an independent check on the scaling model of Table 1.

Figure C3 are also consistent with the scalings in equation (18), although the increase in V is too weak to be resolved. When we compensated the data for this scaling, we found no significant residual trends in either L or V.

[45] We have come to a rather interesting result: on average, larger transform faults have bigger earthquakes but smaller seismic productivities. Through some poorly understood mechanism, the distributions of both small and large earthquakes adjust with the fault area in a way that maintains a constant coupling coefficient χ.

6. Discussion

[46] Our preferred scaling model for RTF seismicity is summarized in Table 1. As a final consistency check, we synthesized a frequency-moment distribution from the model and compared it with the M_W data from the global RTF catalog (Figure 13). The only data used to construct the synthetic distribution were the observed fault lengths L and the slip rates V computed from the NUVEL-1 plate motions; the synthetic distribution was calibrated to the seismicity catalog only through the scaling relations for the upper cutoff moment M_C and the cumulative number of events N_0. The agreement between the synthetic and observed seismicity in Figure 13 is at least as good as the direct fit of the three-parameter model (cf. Figure 6). This global test corroborates the scaling relations inferred from subsets of the data.

[47] The linear thermal scaling relation, $A_E \propto A_T$, implies that seismic coupling χ is independent of L and V. A constant χ would be expected, for example, if the fault rheology were governed by thermally activated transitions from stable to unstable sliding. The simplest model is a "thin" seismic zone, in which both the top and the bottom of the zone conform to isotherms, the area between the isotherms is seismically fully coupled, and the average seismic thickness is thus equal to the effective thickness W_E. An RTF in this configuration conforms to the single-mode hypothesis, which states that a fault patch is either fully seismic or fully aseismic (Appendix A). For typical tectonic values of L = 300 km and V = 40 mm/yr, W_E is only about 1.7 km. If we follow *Burr and Solomon* [1978] in taking the upper boundary of the seismic zone to be the seafloor (Figure 14a), we are stuck with an implausibly shallow basal isotherm (~100°C). As *Bird et al.* [2002] have pointed out, a thin, shallow seismic zone is inconsistent with observed earthquake focal depths and laboratory experiments.

[48] An alternative is a thin, deep seismic zone. Fixing the basal isotherm at 600°C yields an upper boundary for a fully coupled zone at about 520°C (Figure 14b). This boundary

Table 1. Scaling Model for RTF Seismicity[a]

Relation	Seismic Parameter	Scaling With A_T, L, and V
A	seismic coupling	$\chi \propto$ const (≈0.15 for T_{ref} = 600°)
B	effective area	$A_E \propto A_T \propto L^{3/2}V^{-1/2}$
C	cumulative moment	$\Sigma M \propto A_T V \propto L^{3/2}V^{1/2}$
D	upper cutoff area	$A_C \propto A_T^{1/2} \propto L^{3/4}V^{-1/4}$
E	upper cutoff slip	$D_C \propto A_T^{1/4} \propto L^{3/8}V^{-1/8}$
F	upper cutoff moment	$M_C \propto A_T^{3/4} \propto L^{9/8}V^{-3/8}$
G	seismic productivity	$\nu_0 \propto A_T^{-1/4} \propto L^{-3/8}V^{1/8}$
H	cumulative number	$N_0 \propto A_T^{3/4}V \propto L^{9/8}V^{5/8}$

[a]The RTF seismicity data are consistent with the exponents $\beta = 2/3$, $\psi = 1$, $\gamma = 1/2$, and $\lambda = 1/2$, defined in equations (3), (11), (12), and (15), which imply this set of scaling relations.

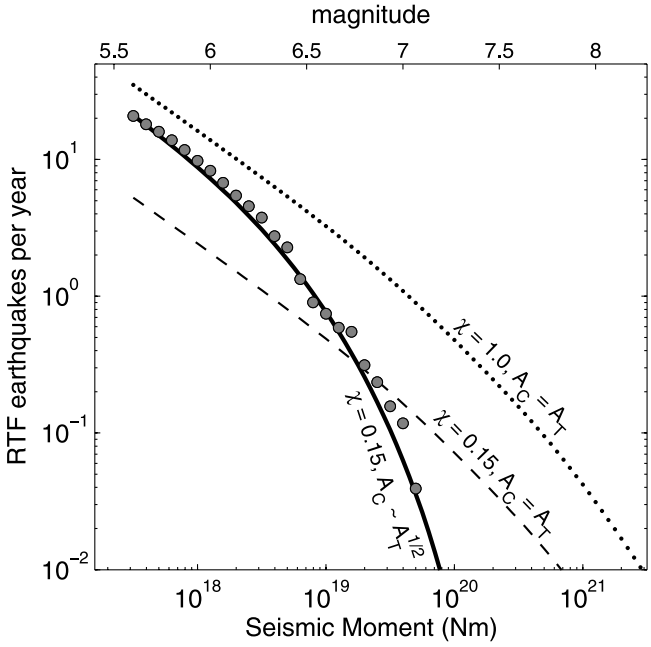

Figure 13. Comparison of the cumulative frequency-moment distribution from the Harvard CMT catalog (solid circles) with three models. The seismicity data are the same as in Figure 6a. The models combine the global distribution of RTF tectonic parameters with seismicity scaling relations; i.e., each fault is assumed to generate seismicity according to equation (3) with $\beta = 2/3$ and the other parameters scaled to its observed fault length L and slip rate V. The dotted curve shows a fully coupled model ($\chi = 1$) with an upper cutoff area equal to the thermal area of contact ($A_C = A_T$). The dashed curve is a similar model with a coupling factor reduced to the observed value ($\chi = 0.15$). The solid curve is a model that satisfies this constraint plus the observed scaling relation $A_C = 3.5\ A_T^{1/2}$. The good fit obtained by the latter corroborates the scaling model of Table 1.

could be related to the stability of serpentinite. Many authors have implicated hydrated ultramafic minerals of the serpentine group in the promotion of subseismic slip. Serpentinized peridotites are commonly dredged from RTFs [*Tucholke and Lin*, 1994; *Cannat et al.*, 1995], and serpentinized Franciscan rocks outcrop on the creeping section of the San Andreas Fault [*Allen*, 1968]. Lizardite and chrysotile, the most common serpentine minerals in oceanic rocks, are stable up to temperatures of about 500°C [*O'Hanley et al.*, 1989]. Velocity-strengthening behavior (stable sliding) has been observed in room temperature laboratory experiments on serpentinite at plate-tectonic slip speeds ($<5 \times 10^{-9}$ m/s) [*Reinen et al.*, 1994]. The presence of serpentinite may therefore inhibit the shallow nucleation of RTF earthquakes.

[49] However, it is unlikely that earthquake ruptures remain confined to a thin, deep seismic zone. *Reinen et al.* [1994] found that serpentinite transforms to velocity-weakening behavior at moderately higher slip rates (10^{-8}–10^{-7} m/s), so earthquakes nucleating within a thin, deep seismic zone could propagate into, and perhaps all the way through, any shallow serpentine-rich layer. Seismic slip and aseismic creep are both observed during experiments on a single, laboratory sample of serpentinite and can be reproduced with spring-slider simulations using a multimechanism constitutive model [*Reinen*, 2000a, 2000b]. This behavior violates the single-mode hypothesis but is consistent with finite source inversions for large RTF earthquakes

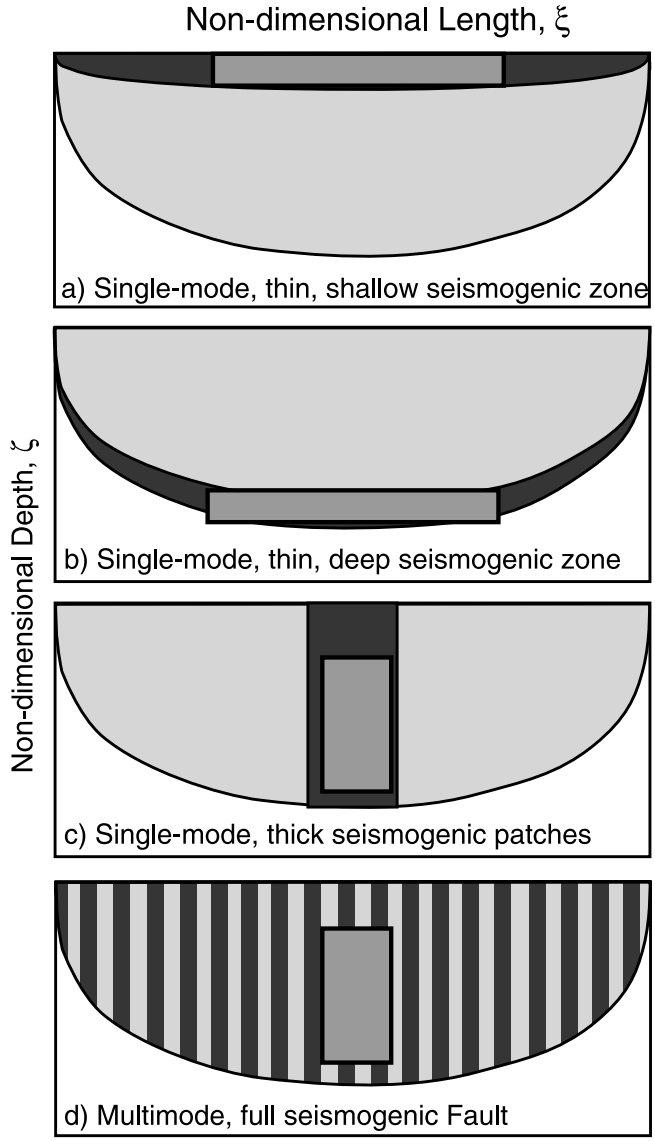

Figure 14. (a)–(c) Schematic models of the RTF seismogenic zone that conform to the scaling relations of Table 1. Models in Figures 14a–14c obey the single-mode hypothesis; the black regions show the fully coupled fault area, equal to A_E, and the light gray regions show the area that slips subseismically, equal to $A_E - A_T$. The medium gray rectangles superposed on the seismogenic zones represent the area of the upper cutoff earthquake, A_C, here scaled to an RTF of intermediate size ($A_T = 2000$ km^2, $A_E = 300$ km^2, $A_C = 155$ km^2). The thin, shallow seismogenic zone in Figure 14a and thin, deep seismogenic zone in Figure 14b are bounded by isotherms, whereas the seismogenic zone in Figure 14c is laterally separated into thick patches. (d) Illustration of a multimode model in which slip can occur seismically or subseismically over the entire thermal area of contact.

Table 2. Oceanic Transform Fault Earthquake Stress Drops

Fault	Date	M, 10^{18} N m	L, km	W_T,[a] km	$\Delta\sigma$, MPa	References
Romanche	14 March 1994	50	112[b]	22	0.4	*McGuire et al.* [2002a]
Romanche	14 March 1994	40	70–120[c]	30[c]	0.2–0.4	*Abercrombie and Ekström* [2001]
Mendocino	1 Sept. 1994	39	75[b]	20[e]	0.7	*McGuire et al.* [2002b]
Romanche	18 May 1995	22	77[b]	22	0.3	*McGuire et al.* [2002b]
Blanco	2 June 2000	2.5	75[d]	10	0.1	*Bohnenstiehl et al.* [2002]

[a]When not otherwise marked, W_T is taken from the thermal widths listed in Table B1.
[b]L is computed from second moments of the moment tensor.
[c]L and W_T are from slip model calculated from waveform inversion.
[d]L is inferred from distribution of aftershocks.
[e]W_T for the Mendicino is inferred from the earthquake focal depth calculations of *Oppenheimer et al.* [1993].

[*Abercrombie and Ekström*, 2001; *McGuire et al.*, 2002b], which indicate that the rupture width of an upper cutoff event, W_C, is probably closer to the full thermal thickness W_T than to W_E.

[50] We therefore consider models in which the seismic zone is wider than W_E but laterally patchy. The area of this zone, which we denote A_S, measures the part of the fault where seismic moment release occurs, so the single-mode hypothesis used in the thin zone models can be expressed by the statement

$$A_S = A_E \tag{19}$$

(single-mode hypothesis). If we make the reasonable assumption that the width of the seismic zone is equal to the width ruptured by the largest probable earthquake ($W_S = W_C$) and use the notation of equation (13) to write the effective length of the seismic zone as $L_S = A_S/\eta W_T$, then the single-mode hypothesis implies $L_S = (\chi/\eta)L$. Assuming $\eta \approx 1$, as inferred from the finite source inversions, $L_S \approx \chi L$, which means that earthquake ruptures on a typical RTF would be confined to only about one sixth of the total fault length (Figure 14c). This model can, in principle, be assessed from the along-strike distribution of RTF ruptures, but the uncertainties in epicenter locations and their relationship to rupture extent preclude a definitive result.

[51] A more diagnostic test of the single-mode hypothesis comes from the requirement that the area ruptured by an upper cutoff earthquake A_C be accommodated within the area of the seismic zone A_S and thus within the effective seismic area A_E:

$$A_C \le A_E \tag{20}$$

(single-mode hypothesis). The observation that $1/2 \approx \gamma < \psi \approx 1$ implies that the power laws (11) and (15) must cross, so we can choose the fiducial point A_T^* such that $A_C^* = A_E^*$. In order to maintain inequality (20) below this crossover, there must be a break in the A_C or A_E scaling relation, or in both, at A_T^*. No obvious scale break is observed in Figures 9 and 10 within the data range 350 km$^2 \le A_T \le$ 21,000 km^2. The single-mode hypothesis thus implies that A_T^* lies outside this range.

[52] The location of the crossover depends on the stress drop. Our preferred scaling model ($\gamma = 1/2$, $\lambda = 1/2$) gives

$$A_T^* = \hat{A}_T^*(\Delta\hat{\sigma}/\Delta\sigma)^{4/3}, \tag{21}$$

where $\hat{A}_T^*$ is computed assuming a reference stress drop of $\Delta\hat{\sigma}$. For $\Delta\hat{\sigma} = 3$ MPa, we obtained the central estimates $A_T^* =$ 555 km^2 from the m_W catalog, and $\hat{A}_T^* = 862$ km^2 from the m_S catalog (cf. Figure 10). Few estimates are available for the static stress drops of RTF earthquakes. This is not too surprising, because the standard teleseismic method for recovering stress drop relies on inferring fault rupture dimensions from aftershock sequences, which cannot be applied to most RTFs owing to the paucity of their aftershocks (Figure 4). An exception is the 27 October 1994 Blanco earthquake, whose small aftershocks were delineated by *Bohnenstiehl et al.* [2002] using SOSUS *T* phase data. We combined their inferred rupture dimension of 75 km with a thermal width of $W_T = 10$ km and the Harvard CMT moment to obtain $\Delta\sigma = 0.1$ MPa (Table 2). The rupture dimensions of a few RTF earthquakes were also available from recent teleseismic waveform inversions. *McGuire et al.* [2002a, 2002b] estimated the second spatial moments of three large events on the Romanche transform fault, which gave us stress drops of 0.3–0.4 MPa. Similar results were found for the 14 March 1994 earthquake using the finite source model published by *Abercrombie and Ekström* [2001].

[53] These data suggest that the stress drops for RTF earthquakes are on the order of 1 MPa or less, so equation (21) implies $A_T^* \ge 4.3\,\hat{A}_T^*$. Taking into account the estimation uncertainties for $\hat{A}_T^*$ yields $A_T^* >$ 480 km^2 (m_W catalog) and >710 km^2 (m_S catalog) at the 95% confidence level. We conclude that the crossover should lie within our data range, but does not, and therefore that the simple power laws derived from the fits shown in Figures 9 and 10 are inconsistent with the single-mode hypothesis. In other words, the rupture areas of large earthquakes on the smaller RTFs appear to be bigger than their effective seismic areas, at least on average.

[54] While there are significant uncertainties in the various parameters and assumptions underlying this test (e.g., constant stress drop), the results are consistent with the inferences drawn by *Reinen* [2000a] from her laboratory data and supports the multimode model shown in Figure 14d in which seismic and subseismic slip can occur on the same fault patch.

7. Conclusions

[55] The RTF scaling relations in Table 1 are complete in the sense that every variable in our seismicity model has been scaled to the two tectonic control parameters fault length L and slip velocity V. The seismicity depends on the fault length and width (depth) only through the thermal area of contact $A_T \propto L^{3/2}V^{-1/2}$; i.e., all of the scaling relations can be written in terms of A_T and V. We have validated this model using multiple seismicity catalogs and an interlock-

ing set of constraints. In particular, the seismic productivity $\nu_0 \propto N_0/A_T V$ was determined indirectly from the data on the larger earthquakes through the moment balance equation (17), as well as directly from counts of (mostly small) earthquakes. These nearly independent estimates of the productivity scaling both deliver relation G of Table 1.

[56] Our scaling model is remarkable in its simplicity and universality. As shown by *Bird et al.* [2002] and confirmed here, RTF earthquakes are well described by a truncated Gutenberg-Richter distribution with a self-similar slope, $\beta = 2/3$. Integrating over this distribution yields a linear thermal scaling for the effective seismic area (relation B), which implies that the seismic coupling coefficient χ is also independent the tectonic parameters (relation A). Thus, while the moment release rates vary by more than an order of magnitude from one fault to another, the seismic coupling for a long, slow fault is, on average, the same as for a short, fast fault. Stated another way, the partitioning between seismic and subseismic slip above T_{ref} does not vary systematically with the maximum age of the lithosphere in contact across the fault, which ranges from about 1 Ma to 45 Ma.

[57] Our results do not support the oft stated view that χ decreases with V [e.g., *Bird et al.*, 2002; *Rundquist and Sobolev*, 2002]. In our model, V governs seismicity only as a tectonic loading rate and through the thermal area of contact (e.g., relations C and H). While laboratory experiments clearly indicate a dependence of fault friction on loading rate, no rate-dependent effects are obvious in the RTF seismicity, and we require no systematic variation in fault properties from slow to fast mid-ocean ridges (e.g., a decrease in the amount of serpentinization with V, as suggested by *Bird et al.* [2002]).

[58] As a global mean, our estimate of seismic coupling is in line with previous studies of RTF seismicity. For a basal reference isotherm $T_{ref} = 600°C$, the data yield $\chi \approx 15\%$ (±5% standard error). If no seismic slip occurs below this reference isotherm, then nearly six sevenths of the slip above it must be accommodated by subseismic mechanisms not included in the cataloged moment release: steady aseismic creep, silent earthquakes, and infraseismic (quiet) events.

[59] Relation B suggests that temperature is the main variable controlling the distribution of seismic and subseismic slip. However, by combining relations B and D with observations of low stress drop, we find that the area ruptured by the largest expected earthquake exceeds the effective seismic area ($A_C > A_E$) for the smaller RTFs. This inequality violates the "single-mode hypothesis," which states that a fault patch is either fully seismic or fully aseismic. If this inference is correct, then the small value of χ and its lack of dependence on L and V cannot simply reflect the thermal state of the faulting; some sort of temperature-dependent mechanics must govern the multimode partitioning of seismic and subseismic slip.

[60] A dynamical rather than structural control of ridge transform faulting is underscored by a basic conclusion of our study: on average, larger RTFs have bigger earthquakes but smaller seismic productivities, and the two corresponding seismicity parameters, A_C and ν_0, trade off to maintain constant seismic coupling. Moreover, the areal scaling of the biggest RTF earthquakes (relation D) is characterized by an exponent that lies halfway between the zero value implied by a constant upper cutoff moment (advocated for global seismicity by *Kagan* [2002b]) and the unit value of a simple linear model. An increase of A_C with A_T is hardly surprising, since larger faults should support larger earthquakes, but the square root scaling indicates heterogeneities in stress and/or fault structure (e.g., segmentation) that act to suppress the expected linear growth of A_C with A_T (see comparison in Figure 13).

[61] These heterogeneities might plausibly arise from a dynamical instability in the highly nonlinear mechanics of fault growth. Fault lengths in various tectonic settings are observed to increase in proportion to cumulative slip, $L \propto \Sigma D$ [*Elliott*, 1976; *Cowie and Scholz*, 1992; *Cowie*, 1998], and the coalescence of neighboring faults leads to the localization of displacement on smoother, longer faults with larger earthquakes [*Stirling et al.*, 1996; *Scholz*, 2002]. In the case of RTFs, where the cumulative displacements can reach thousands of kilometers, the tendency toward localization must be counterbalanced by mechanical instabilities that prevent "ridge-to-ridge" ruptures and maintain the relation D over order-of-magnitude variations in L and V.

[62] This mechanics is no doubt intrinsically three-dimensional, involving interactions among multiple strands within the transform fault system. Extensional relay zones and intratransform spreading centers develop due to changes in plate motion [*Bonatti et al.*, 1994; *Pockalny et al.*, 1997; *Ligi et al.*, 2002]. Some RTF earthquake sequences show ruptures on parallel faults offset by tens of kilometers [*McGuire et al.*, 1996; *McGuire and Jordan*, 2000; *McGuire et al.*, 2002a], which may reflect the cross-strike dimension of the system. A power law distribution of faults below this outer scale may explain the self-similar GR distribution observed for small earthquakes, as well as the self-similar slip distribution inferred for large earthquakes (relation E). However, the earthquake-mediated stress interactions among these faults must be very weak to satisfy the low branching ratio ($n \approx 0.1$) we observed for RTF aftershock sequences. In other words, the subseismic slip that accounts for nearly 85% of the total moment release also drives about 90% of rupture nucleation.

[63] Given the evidence for slow precursors to many large RTF earthquakes [*Ihmlé and Jordan*, 1994; *McGuire et al.*, 1996; *McGuire and Jordan*, 2000], we speculate that the seismogenic stresses on ridge transform faults may be primarily regulated by slow transients, rather than the fast ruptures that dominate continental strike-slip faults. In this view, most ordinary (loud) earthquakes on RTFs would simply be "aftershocks" of quiet or silent events.

Appendix A: San Andreas Fault Model

[64] According to this hypothetical model of continental strike-slip faulting, essentially all permanent strain within the seismogenic zone occurs as seismic slip (i.e., the faults are seismically "fully coupled" [*Brune*, 1968; *Kiratzi*, 1993; *Stein and Hanks*, 1998]) except along rare creeping segments where most of the strain is accommodated aseismically [*Schulz et al.*, 1982; *Thatcher*, 1990; *Scholz*, 2002]. This behavior, which we refer to as the "single-mode hypothesis," is maintained in the transition from the locked to creeping sections, which are populated with isolated,

Table B1. Tectonic and Seismic Data for Oceanic Ridge Transform Faults

Fault Reference	Name	Latitude	Longitude	L, km	V, mm/yr	m_b	m_S	m_W	ΣM, 10^{18} N m	χ	W_T, km	z_{max}, km	A_T, km^2	A_E, km^2	A_C, km^2
					Mid-Atlantic Ridge										
1	Jan Mayen	71.3	350.9	220	17.3	6.0	5.6	6.0	3.5	0.06	14.5	17.2	3148	180	52
2	Charlie Gibbs (A)	52.7	326.6	220	22.4	5.9	6.5	6.7	15.4	0.22	12.7	15.1	2762	612	288
3	Charlie Gibbs (B)	52.2	329.1	120	15.9	5.2	5.4	5.4	0.4	0.02	11.5	13.6	1430	22	12
4	Oceanographer	35.1	324.4	120	22.0	5.7	6.0	6.3	9.6	0.33	9.7	11.5	1188	387	111
5	Hayes	33.6	321.4	140	22.6	5.8	5.8	6.1	3.1	0.08	10.3	12.2	1470	120	71
6	Atlantis	30.1	317.6	80	23.6	5.8	6.0	5.5	0.2	0.01	7.7	9.2	643	8	17
7	Kane	23.8	314.4	140	25.2	6.1	6.4	6.4	10.0	0.26	9.6	11.4	1339	353	147
8	15′20″	15.4	314.2	200	26.4	5.8	4.9	5.4	0.2	0.00	11.4	13.5	2323	8	14
9	Vema	10.9	317.7	330	28.2	6.1	6.9	6.9	53.2	0.37	14.0	16.6	4573	1679	462
10	Doldrums	7.6	323.1	650	29.3	6.3	7.0	7.0	51.0	0.12	19.3	22.9	12562	1549	565
11	St Paul	0.6	332.4	540	31.9	6.1	6.5	6.6	40.1	0.12	16.9	20.1	9225	1119	236
12	Romanche	−0.3	339.4	920	32.5	6.2	6.7	7.1	195.0	0.27	21.8	25.9	20058	5327	700
13	Chain	−1.2	345.5	320	33.0	6.3	7.0	6.8	56.4	0.38	12.7	15.1	4050	1521	354
14	Ascension	−11.7	346.3	160	35.0	5.3	6.1	6.2	4.2	0.08	8.6	10.3	1350	108	93
15	MAR 35S	−35.4	343.5	240	35.5	6.0	6.4	6.6	36.6	0.37	10.6	12.6	2503	916	221
16	Falkland	−47.2	348.1	250	33.4	5.3	5.9	6.0	2.6	0.02	11.2	13.3	2810	70	58
					Juan De Fuca										
17	Blanco	43.8	231.5	360	59.4	6.1	6.3	6.4	23.3	0.10	10.1	12.0	3660	348	149
					East Pacific Rise										
18	Rivera	19.0	252.6	460	71.2	6.1	6.8	6.9	70.4	0.18	10.4	12.4	4771	880	440
19	Orozco	15.2	255.0	90	86.5	5.1	5.1	5.6	0.3	0.01	4.2	5.0	384	4	24
20	Clipperton[a]	10.2	256.0	90	105.3	5.7	6.5	6.6	19.8	0.53	3.7	4.4	313	167	213
21	Siqueiros	8.4	256.5	150	111.9	5.2	5.7	5.9	5.3	0.06	4.7	5.6	712	42	43
22	Quebrada	−3.8	256.8	120	137.4	5.2	5.3	5.6	0.7	0.01	3.9	4.6	474	5	23
23	Discovery[a]	−4.0	255.8	70	137.9	5.1	5.8	6.0	6.3	0.19	3.0	3.5	214	41	56
24	Gofar	−4.5	254.6	190	138.8	5.9	5.9	6.2	16.9	0.12	4.8	5.7	902	108	86
25	Yaquina[a]	−6.2	252.8	60	141.4	5.1	5.2	5.5	0.5	0.02	2.6	3.0	142	3	18
26	Wilkes	−9.0	251.0	200	145.0	5.3	5.7	5.9	3.1	0.02	4.8	5.7	954	19	42
27	Garrett	−13.4	248.2	120	149.8	5.3	5.8	5.8	3.5	0.05	3.7	4.3	434	20	35
					Chile Rise										
28	Chile	−35.5	256.8	1120	58.8	5.8	6.6	6.7	88.7	0.07	17.9	21.3	20064	1342	296
29	Valdivia	−41.5	271.2	530	60.0	5.6	5.5	5.9	4.6	0.01	12.1	14.4	6379	69	44
					Pacific Antarctic Ridge										
30	Menard	−49.6	244.7	210	90.5	5.9	6.1	6.4	20.0	0.15	6.3	7.5	1347	197	142
31	Vacquier[a]	−53.1	241.8	80	87.2	5.3	5.6	5.8	2.2	0.07	4.0	4.7	322	22	34
32	Raitt	−54.5	240.5	140	85.8	5.6	5.9	6.0	2.4	0.03	5.3	6.3	756	25	58
33	Heezen	−55.7	235.5	350	83.8	5.7	6.3	6.4	27.4	0.10	8.4	9.9	2927	291	139
34	Tharp	−54.6	229.0	430	83.5	5.6	6.1	6.2	19.8	0.05	9.3	11.0	3991	211	95
35	Hollister	−54.4	223.9	120	82.5	5.6	6.5	6.4	16.6	0.31	4.9	5.8	577	179	146
36	Herron[a]	−56.5	220.8	60	79.7	5.5	5.7	5.9	1.2	0.07	3.5	4.2	210	14	42
37	Udintsev	−56.5	217.6	270	78.8	5.8	6.0	6.4	16.0	0.09	7.6	9.0	2034	181	141
					America Antarctic Ridge										
38	Bullard (A)	−59.1	342.8	90	17.2	5.4	5.5	5.8	1.8	0.11	9.3	11.0	822	94	37
39	Bullard (B)	−58.2	348.1	510	17.5	6.0	6.2	6.4	17.2	0.08	22.1	26.3	11334	872	144
40	Conrad	−55.7	356.7	190	18.5	5.7	6.4	6.7	17.0	0.33	13.1	15.6	2480	816	290
					South West Indian Ridge										
41	Bouvet	−54.2	1.9	200	13.8	5.8	6.5	6.6	11.3	0.24	15.4	18.3	3017	730	210
42	Islas Orcadas	−54.2	6.1	110	14.0	5.8	5.6	5.6	0.5	0.02	11.5	13.7	1266	29	22
43	Shaka	−53.5	9.3	210	14.1	5.7	5.9	6.4	6.4	0.12	15.9	18.9	3393	403	137
44	Du Toit	−53.0	25.5	120	14.6	5.2	5.9	6.2	3.8	0.17	11.7	13.9	1378	228	95
45	Andrew Bain	−50.1	30.0	650	14.6	6.8	6.7	6.4	13.6	0.05	27.4	32.6	17944	826	150
46	Marion	−46.6	33.7	120	14.7	5.4	5.6	5.8	0.6	0.03	11.5	13.6	1323	36	34
47	Prince Edward	−45.4	35.1	160	14.7	5.5	5.5	5.9	1.5	0.04	13.7	16.3	2264	92	41
48	Eric Simpson[a]	−43.5	39.3	60	14.8	5.5	6.4	6.7	14.0	1.79	8.1	9.6	469	839	270
49	Discovery II (A)	−43.4	41.6	140	14.8	5.4	5.9	6.4	10.1	0.36	12.4	14.7	1682	606	139
50	Discovery II (B)	−41.9	42.5	190	14.8	5.7	6.2	6.7	14.7	0.31	14.7	17.5	2831	883	288
51	Indomed	−39.5	46.1	120	14.8	5.9	5.8	5.8	1.7	0.07	11.8	14.1	1461	101	38
52	Atlantis II	−32.8	57.0	200	14.6	5.7	5.8	5.4	0.4	0.01	5.2	18.0	3035	27	15
					Central Indian Ridge										
53	Gemino[a]	−22.9	69.2	60	47.3	5.3	5.2	5.2	0.2	0.01	4.5	5.3	253	3	8
54	Marie Celeste	−17.4	65.9	210	40.8	5.6	6.0	6.5	40.4	0.46	9.2	10.9	1899	880	173
55	Argo	−13.7	66.3	120	37.6	5.6	5.6	6.0	3.4	0.10	7.2	8.6	838	81	50
56	CIR 12′12″	−11.9	65.7	150	35.5	6.0	6.1	6.1	3.7	0.08	8.3	9.9	1221	92	62
57	Vema II	−8.9	67.5	210	34.0	5.6	5.7	6.2	4.4	0.05	10.2	12.2	2169	116	79

Table B1. (continued)

Fault Reference	Name	Latitude	Longitude	L, km	V, mm/yr	m_b	m_S	m_W	ΣM, 10^{18} N m	χ	W_T, km	z_{max}, km	A_T, km^2	A_E, km^2	A_C, km^2
					Gulf of Aden										
58	Alula Fartak	13.9	51.7	200	19.4	5.9	5.5	5.9	3.2	0.06	13.1	15.5	2588	147	47
59	Owen	11.5	57.5	310	23.9	6.2	6.2	6.5	29.2	0.23	14.9	17.7	4682	1085	162
					South East Indian Ridge										
60	Ter Tholen	−33.2	77.8	100	65.2	5.5	5.4	5.2	0.1	0.00	5.1	6.1	518	2	9
61	Zeewolf[a]	−35.4	78.5	70	66.4	5.0	4.9	5.3	0.2	0.01	4.1	4.9	272	3	11
62	Amsterdam	−36.6	78.6	80	67.0	5.7	6.0	6.1	8.3	0.29	4.6	5.5	386	110	67
63	Boomerang[a]	−37.4	78.2	40	67.2	5.2	6.0	5.7	0.6	0.05	3.3	3.9	139	7	29
64	Hillegom's Hole[a]	−38.5	78.6	40	67.8	5.7	6.3	6.4	9.8	0.97	3.2	3.8	132	128	150
65	Vlamingh	−41.5	80.2	140	69.4	5.8	6.3	6.4	21.5	0.35	5.7	6.8	777	275	154
66	Geelvinck	−41.7	85.0	150	70.8	5.6	5.3	5.4	0.6	0.01	5.9	7.1	888	8	15
67	SEIR 88E	−42.0	88.3	90	71.7	5.4	5.7	5.7	1.3	0.04	4.5	5.4	401	16	30
68	SEIR 96E (A)[a]	−45.6	96.1	70	73.9	5.8	6.2	6.3	9.7	0.42	4.0	4.7	281	117	100
69	SEIR 96E (B)[a]	−46.5	95.9	50	74.0	5.3	5.7	5.7	1.6	0.12	3.3	3.9	156	20	27
70	SEIR 100E	−47.8	99.8	130	74.7	5.5	6.3	6.4	13.3	0.23	5.4	6.4	686	159	139
71	SEIR 107E	−48.8	106.5	130	75.3	5.2	5.2	5.5	0.4	0.01	5.4	6.4	705	5	16
72	SEIR 114E[a]	−50.0	114.1	70	75.4	5.3	5.4	5.4	0.4	0.02	4.0	4.7	277	4	15
73	Euroka	−49.2	126.1	120	74.6	5.3	5.6	5.5	1.0	0.02	5.3	6.3	657	12	19
74	Birubi	−49.3	127.4	130	74.4	5.6	5.0	5.4	0.3	0.01	5.5	6.5	723	4	14
75	George V	−52.0	139.8	480	72.0	5.9	6.4	6.5	42.8	0.10	10.6	12.6	5071	528	191
76	SEIR 143E	−54.5	143.8	100	71.0	5.4	5.8	5.8	4.3	0.11	4.9	5.9	511	54	37
77	Tasman	−57.8	147.7	690	70.1	5.8	6.4	6.5	60.9	0.09	12.8	15.2	8773	772	195
78	Balleny	−61.5	154.4	350	69.0	5.7	6.7	6.7	64.3	0.25	9.3	11.0	3275	829	270
Total	-	-	-	17,230	-	-	-	-	1270	-	-	-	215,978	30,186	9646

[a]RTF has been excluded from general analysis because $L < 75$ km or $A_T < 350$ km^2.

fully coupled patches surrounded by continuously creeping material [e.g., *Lindh and Boore*, 1981; *Harris and Segall*, 1987; *Nadeau and Johnson*, 1998; *Sammis and Rice*, 2001; *Waldhauser and Ellsworth*, 2002]. Slow strain transients with time constants of hours to days (silent earthquakes) do occur, but they are small and infrequent and appear to be associated with the creeping parts [*Gladwin et al.*, 1994; *Linde et al.*, 1996; *Thurber and Sessions*, 1998]. Slow earthquakes (seismic events with anomalous low-frequency excitation suggestive of low rupture velocities) are also rare [*Kanamori and Hauksson*, 1992; *Ihmlé and Jordan*, 1994]; the large events that have been studied in detail show rupture velocities that approach (or sometimes exceed) the shear wave speed [e.g., *Aki*, 1968; *Beroza*, 1991; *Wald et al.*, 1996; *Bouchon et al.*, 2000]. Fault area is fractally distributed within the volume of continental crust [*Turcotte*, 1986; *Aviles et al.*, 1987; *King et al.*, 1988; *Hirata*, 1989; *Power and Tullis*, 1995; *Ouilion et al.*, 1996]; as the displacement increases, this distribution evolves through a process of strain localization to produce smoother, longer faults with larger characteristic earthquakes [*Wesnousky*, 1990; *Stirling et al.*, 1996]. According to this hypothesis, geologic structure plays a dominant role in determining earthquake complexity. This complexity is reflected in aftershock sequences, which follow a modified version of Omori's law [*Utsu*, 1961; *Reasenberg and Jones*, 1989; *Kisslinger and Jones*, 1991] and conform to Båth's law, namely, that the largest aftershock is about 1.2 magnitude units lower than the main shock [*Båth*, 1965; *Felzer et al.*, 2002; *Helmstetter and Sornette*, 2003a]. The largest earthquakes result from event cascades that involve the propagation of faulting across segment boundaries and are thus larger than the characteristic earthquakes for individual segments [*Jackson*, 1996; *Ward*, 1997]. The best data indicate that the slip displacement D scales with the rupture length L and width W as $S = \sqrt{LW}$ (the self-similar or S model), even for large earthquakes that rupture through the entire seismogenic zone [*Mai and Beroza*, 2000; P. Somerville, personal communication, 2003].

Appendix B: RTF Tectonic Parameters and Seismic Data

[65] Table B1 is a compilation of observed and calculated measures of RTF location, size, and seismicity. Latitude and longitude values indicate the midpoint of each RTF. V was calculated from the NUVEL-1 plate velocity model [*DeMets et al.*, 1990]. Magnitudes are the maximum value reported in the 36 year (1964–1999) ISC catalog (for m_b and m_S data), or the 25.5 year (June 1976 to January 2002) CMT catalog (for m_W data). ΣM indicates the total moment release reported by the CMT catalog for each RTF. The reference isotherm $T_{ref} = 600°C$ was used to compute χ, W_T, z_{max}, and A_T. A stress drop of $\Delta\sigma = 3$ MPa was assumed in the calculation of A_C. Faults were split into multiple segments if there was an offset $\geq$35 km.

Appendix C: Scaling of Seismic Parameters With L and V

[66] Figures C1–C3 display how the seismicity parameters total moment release ΣM, upper cutoff earthquake moment M_C, and seismic productivity ν_0 are distributed with the tectonic parameters fault length L and slip rate V. The diamonds correspond to the maximum likelihood estimates derived from the binned Harvard CMT data with $m_0 = 5.6$ and $\beta = 2/3$; the circles are the observations for individual RTFs. In calculating the ordinate values for the maximum likelihood estimates, we weighted the individual faults by their theoretical moment rates, which are proportional to VA_T. In comparisons with the maximum likelihood estimates of M_C, we used the largest seismic moment

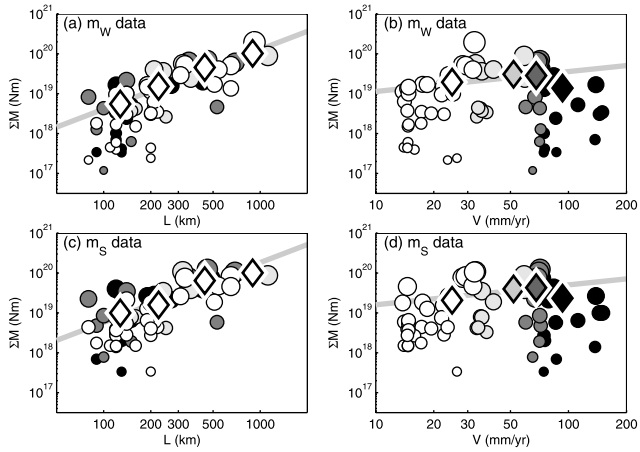

Figure C1. (left) Total seismic moment ΣM verses fault length L and (right) slip rate V for (top) the Harvard CMT catalog and (bottom) recalibrated ISC m_S catalog. Points show cumulative moments for individual RTFs (circles) and maximum likelihood estimates obtained by fitting equation (4) to the binned data (diamonds). The data bins, as well as the circle sizes and shading, are given in Figure 5. The abscissa values for the diamonds are the averages of L and V in each bin weighted by the plate tectonic moment release rate $\mu A_T V$. Solid lines correspond to the model scaling relation, $\Sigma M \sim L^{3/2} V^{1/2}$ (Table 1).

observed on an individual RTF. The maximum likelihood estimates of the seismic parameters show systematic correlations with fault length, and less convincing trends with slip velocity. As discussed in the text, a proper interpretation

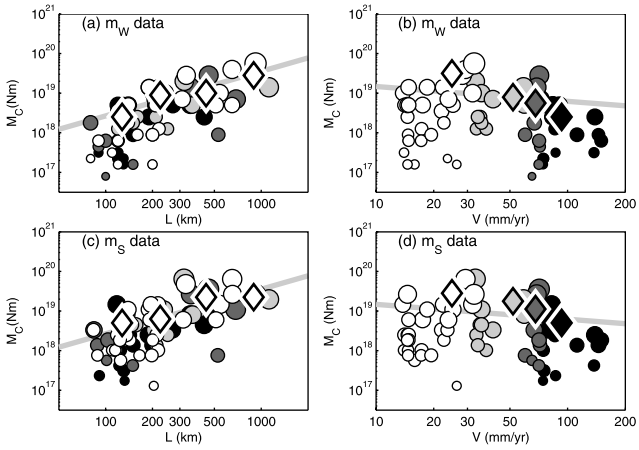

Figure C2. Upper cutoff moment M_C versus (left) fault length L and (right) slip rate V for (top) the Harvard CMT catalog and (bottom)recalibrated ISC m_S catalog. Points show the largest earthquakes for individual RTFs (circles) and maximum likelihood estimates obtained by fitting equation (4) to the binned data (diamonds). The data bins, as well as the circle sizes and shading, are given in Figure 5. The abscissa values for the diamonds are the averages of L and V in each bin weighted by the plate tectonic moment release rate $\mu A_T V$. Solid lines correspond to the model scaling relation, $M_C \sim L^{9/8} V^{-3/8}$, given in Table 1.

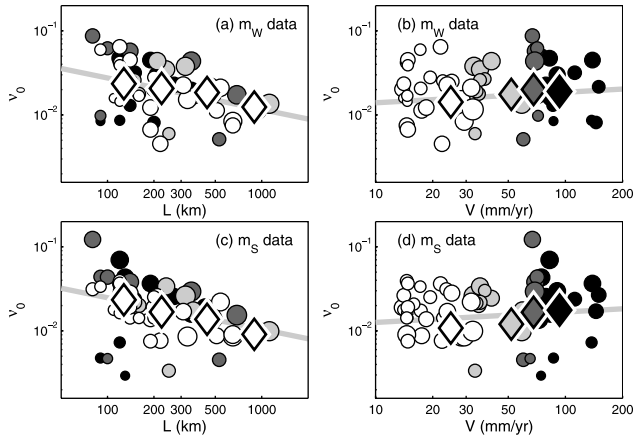

Figure C3. Seismic productivity, $\nu_0 = \dot{N}_0 M_0/(\mu V A_T)$, versus (left) fault length L and (right) slip rate V for (top) the Harvard CMT catalog and (bottom) recalibrated ISC m_S catalog. Points show normalized event counts for individual RTFs (circles) and maximum likelihood estimates obtained by fitting equation (4) to the binned data (diamonds). The data bins, as well as the circle sizes and shading, are given in Figure 5. The ν_0 values from both catalogs have been normalized to a threshold moment magnitude of $m_0 = 5.6$. The abscissa values for the diamonds are the averages of L and V in each bin weighted by the plate tectonic moment release rate $\mu A_T V$. Solid lines correspond to the model scaling relation, $\nu_0 \sim L^{-3/8} V^{1/8}$ (Table 1).

of these relationships must account for any covariance of L and V.

Notation

A_C	upper cutoff area (M_C rupture area).
A_E	effective seismic area (area displaced by the observed moment release rate per unit tectonic slip).
A_S	total fault area from which seismic moment is released.
A_T	thermal area above isotherm T_{ref}.
b	slope of Gutenberg-Richter distribution.
D_C	average slip of upper cutoff earthquake.
ΣD	cumulative slip.
L	fault length.
L_C	fault length ruptured by M_C.
L_S	effective seismic zone length (A_S/W_S).
m_b	body wave magnitude.
m_C	upper cutoff magnitude.
m_{main}	main shock magnitude.
m_S	surface wave magnitude.
m_W	moment magnitude.
m_0	catalog completeness threshold magnitude.
m_Σ	cumulative moment magnitude.
Δm_{after}	magnitude decrement of largest probable aftershock.
M	earthquake moment.
$\dot{M}$	moment release rate.
M_C	upper cutoff moment (largest probable earthquake).
M_0	catalog completeness threshold moment.

ΔM_k moment width of the kth bin.
ΣM total moment release.
n ETAS branching ratio.
n_k number of events in the kth bin.
N cumulative number of earthquakes.
N_{after} number of aftershocks with $m_0 \leq m \leq m_{\text{main}}$.
N_0 number of events above M_0.
$\dot{N}_0$ average N_0 per unit time.
Δt_{cat} duration of earthquake catalog.
T_0 mantle potential temperature.
T_{ref} temperature of a reference isotherm.
V tectonic slip rate.
W_{C} down-dip width ruptured by M_{C}.
W_{E} effective seismic width (A_{E}/L).
W_{S} down-dip width of A_{S}.
W_{T} average depth to T_{ref} (A_{T}/L).
x along strike position.
z down-dip position.
$z_{\max}$ maximum depth to T_{ref}.
α ETAS parameter describing aftershock rate changes with m_{main}.
β low moment slope of the moment-frequency distribution ($\beta = 2/3b$).
γ A_{C} to A_{T} scaling exponent.
ζ nondimensional depth.
η scale factor between W_{C} and W_{T}.
κ thermal diffusivity.
λ slip scaling exponent.
μ shear modulus.
ν_0 seismic productivity.
ξ nondimensional length.
$\Delta\sigma$ stress drop.
$\Delta\hat{\sigma}$ constant stress drop value.
χ seismic coupling coefficient.
ψ A_{E} to A_{T} scaling exponent.

[67] **Acknowledgments.** We thank J. McGuire and G. Hirth for helpful discussions. Comments from reviewers R. Abercrombie, D. Forsyth, and C. Frohlich helped to clarify the paper. M.B. was supported by a NSF Graduate Research Fellowship, a MIT Presidential Fellowship, and the WHOI DOEI Fellowship. This research was supported by the Southern California Earthquake Center. SCEC is funded by NSF Cooperative Agreement EAR-0106924 and USGS Cooperative Agreement 02HQAG0008. This is SCEC contribution 768 and the Woods Hole Oceanographic Institution contribution 11132.

References

Abercrombie, R., and G. Ekström (2001), Earthquake slip on oceanic transform faults, *Nature*, *410*, 74–77.

Abercrombie, R. E., and G. Ekström (2003), A reassessment of the rupture characteristics of oceanic transform earthquakes, *J. Geophys. Res.*, *108*(B5), 2225, doi:10.1029/2001JB000814.

Aki, K. (1956), Some problems in statistical seismology, *J. Seismol. Soc. Jpn.*, *8*, 205–228.

Aki, K. (1965), Maximum likelihood estimate of b in the formula $\log n = a - bm$ and its confidence limits, *Bull. Earthquake Res. Inst. Univ. Tokyo*, *43*, 237–239.

Aki, K. (1968), Seismic displacements near a fault, *J. Geophys. Res.*, *73*, 5959–5976.

Allen, C. R. (1968), The tectonic environments of seismically active and inactive areas along the San Andreas Fault system, in *Proceedings of a Conference on the Geologic Problems of the San Andreas Fault System*, pp. 70–82, Stanford Univ. Press, Stanford, Calif.

Anderson, J. G., and J. E. Luco (1983), Consequences of slip rate constraints on earthquake occurrence relation, *Bull. Seismol. Soc. Am.*, *73*, 471–496.

Aviles, C. A., C. H. Scholz, and J. Boatwright (1987), Fractal analysis applied to characteristic segments of the San Andreas Fault, *J. Geophys. Res.*, *92*, 331–344.

Båth, M. (1965), Lateral inhomogeneities in the upper mantle, *Tectonophysics*, *2*, 483–514.

Behn, M. D., J. Lin, and M. T. Zuber (2002), Evidence for weak oceanic transform faults, *Geophys. Res. Lett.*, *29*(24), 2207, doi:10.1029/2002GL015612.

Bender, B. (1983), Maximum likelihood method estimation of b values for magnitude grouped data, *Bull. Seismol. Soc. Am.*, *73*, 831–851.

Bergman, E. A., and S. C. Solomon (1988), Transform fault earthquakes in the North Atlantic: Source mechanisms and depth of faulting, *J. Geophys. Res.*, *93*, 9027–9057.

Beroza, G. (1991), Near-source modeling of the Loma Prieta earthquake: Evidence for heterogeneous slip and implications for earthquake hazard, *Bull. Seismol. Soc. Am.*, *81*, 1603–1621.

Beroza, G. C., and T. H. Jordan (1990), Searching for slow and silent earthquakes using free oscillations, *J. Geophys. Res.*, *95*, 2485–2510.

Bird, P., Y. Y. Kagan, and D. D. Jackson (2002), Plate tectonics and earthquake potential of spreading ridges and oceanic transform faults, in *Plate Boundary Zones*, *Geodyn. Ser.*, vol. 30, edited by S. Stein and J. T. Freymueller, pp. 203–218, AGU, Washington, D. C.

Bodin, P., and J. M. Brune (1996), On the scaling of slip with rupture length for shallow strike-slip earthquakes: Quasi-static models and dynamic rupture propagation, *Bull. Seismol. Soc. Am.*, *86*, 1292–1299.

Boettcher, M. S., G. Hirth, and B. Evans (2003), Olivine friction at the base of the seismogenic zone, *Eos Trans. AGU*, *84*(46), Fall Meet. Suppl., Abstract T41C-0231.

Bohnenstiehl, D. R., M. Tolstoy, R. P. Dziak, C. G. Fox, and D. K. Smith (2002), Aftershock sequences in the mid-ocean ridge environment: An analysis using hydroacoustic data, *Tectonophysics*, *354*, 49–70.

Bohnenstiehl, D. R., M. Tolstoy, and E. Chapp (2004), Breaking into the plate: A 7.6 M_w fracture-zone earthquake adjacent to the Central Indian Ridge, *Geophys. Res. Lett.*, *31*, L02615, doi:10.1029/2003GL018981.

Bonatti, E., M. Ligi, L. Gasperini, A. Peyve, Y. Raznitsin, and Y. Chen (1994), Transform migration and vertical tectonics at the Romanche fracture zone, equatorial Atlantic, *J. Geophys. Res.*, *99*, 21,779–21,802.

Bouchon, M., N. Toksoz, H. Karabulut, M.-P. Bouin, M. Dietrich, M. Aktar, and M. Edie (2000), Seismic imaging of the Izmit rupture inferred from near-fault recordings, *Geophys. Res. Lett.*, *27*, 3013–3016.

Bowan, J., and R. S. White (1994), Variation with spreading rate of oceainc crustal thickness and geochemistry, *Earth Planet. Sci. Lett.*, *121*, 435–449.

Brune, J. N. (1968), Seismic moment, seismicity, and rate of slip along major fault zones, *J. Geophys. Res.*, *73*, 777–784.

Burr, N. C., and S. C. Solomon (1978), The relationship of source parameters of oceanic transform earthquakes to plate velocity and transform length, *J. Geophys. Res.*, *83*, 1193–1205.

Cande, S., J. LaBrecque, R. Larson, W. Pitman III, X. Golovchenko, and W. Haxby (1989), Magnetic lineations of world's ocean basins (map), technical report, Am. Assoc. of Pet. Geol., Tulsa, Okla.

Cannat, M., et al. (1995), Thin crust, ultramafic exposures, and rugged faulting patterns at the Mid-Atlantic Ridge (22°–24°N), *Geology*, *23*, 49–52.

Cowie, P. A. (1998), Normal fault growth in three-dimensions in continental and oceanic crust, in *Faulting and Magmatism at Mid-Ocean Ridges*, *Geophys. Monogr. Ser.*, vol. 106, edited by W. R. Buck et al., pp. 325–348, AGU, Washington, D. C.

Cowie, P. A., and C. H. Scholz (1992), Physical explanation for displacement-length relationship for faults using a post-yield fracture mechanics model, *J. Struct. Geol.*, *14*, 1133–1148.

Davies, G. F., and J. N. Brune (1971), Regional and global fault slip rates from seismicity, *Nature Phys. Sci.*, *229*, 101–107.

DeMets, C., R. G. Gordon, D. F. Angus, and S. Stein (1990), Current plate motions, *Geophys. J. Int.*, *101*, 425–478.

Dragert, H., K. Wang, and T. S. James (2001), A silent slip event on the deeper Cascadia subduction interface, *Science*, *292*, 1525–1528.

Dziak, R. P., C. G. Fox, and R. W. Embley (1991), Relationship between the seismicity and the geologic structure of the Blanco Transform Fault Zone, *Mar. Geophys. Res.*, *13*(3), 203–208.

Dziak, R., C. Fox, R. Embley, J. Lupton, G. Johnson, W. Chadwick, and R. Koski (1996), Detection of and response to a probable volcanogenic *T*-wave event swarm on the western Blanco Transform Fault Zone, *Geophys. Res. Lett.*, *23*, 873–876.

Dziak, R. P., C. Fox, R. Embley, J. Nabelek, J. Braunmiller, and R. Koski (2000), Recent tectonics of the Blanco Ridge, eastern Blanco Transform Fault Zone, *Mar. Geophys. Res.*, *21*(5), 423–450.

Dziewonski, A. M., and D. L. Anderson (1981), Preliminary Reference Earth Model, *Phys. Earth Planet. Inter.*, *25*, 297–356.

Ekström, G., and A. M. Dziewonski (1988), Evidence of bias in estimations of earthquake size, *Nature*, *332*, 319–323.

Elliott, D. (1976), The energy balance and deformation mechanisms of thrust sheets, *Philos. Trans. R. Soc. London, Ser. A*, *283*, 289–312.

Embley, R. W., and D. S. Wilson (1992), Morphology of the Blanco Transform Fault Zone-NE Pacific—Implications for its tectonic evolution, *Mar. Geophys. Res.*, *14*(1), 25–45.

Engeln, J. F., D. A. Weins, and S. Stein (1986), Mechanisms and depths of Atlantic transform earthquakes, *J. Geophys. Res.*, *91*, 548–577.

Felzer, K. R., T. W. Becker, R. E. Abercrombie, G. Ekström, and J. R. Rice (2002), Triggering of the 1999 M_w 7.1 Hector Mine earthquake by aftershocks of the 1992 M_w 7.3 Landers earthquake, *J. Geophys. Res.*, *107*(B9), 2190, doi:10.1029/2001JB000911.

Forsyth, D. W., Y. Yang, M. Mangriotis, and Y. Shen (2003), Coupled seismic slip on adjacent oceanic transform faults, *Geophys. Res. Lett.*, *30*(12), 1618, doi:10.1029/2002GL016454.

Francis, T. J. G. (1968), The detailed seismicity of mid-ocean ridges, *Earth Planet. Sci. Lett.*, *4*(1), 39–46.

Frohlich, C., and K. D. Apperson (1992), Earthquake focal mechanisms, moment tensors, and the consistency of seismic activity near plate boundaries, *Tectonics*, *11*(2), 279–296.

Frohlich, C., and S. Davis (1993), Teleseismic *b* values; or, much ado about 1.0, *J. Geophys. Res.*, *98*, 631–644.

Gardner, J., and L. Knopoff (1974), Is the sequence of earthquakes in southern California, with aftershocks removed, Poissonian?, *Bull. Seismol. Soc. Am.*, *64*, 1363–1367.

Gladwin, M. T., R. L. Gwyther, R. H. G. Hart, and K. S. Breckenridge (1994), Measurments of the strain field associated with episodic creep events on the San Andreas Fault at San Juan Bautista, California, *J. Geophys. Res.*, *99*, 4559–4565.

Guo, Z., and Y. Ogata (1997), Statistical relations between the parameters of aftershocks in time, space, and magnitude, *J. Geophys. Res.*, *102*, 2857–2873.

Hanks, T. C., and W. H. Bakun (2002), A bilinear source-scaling model for $m - \log a$ observations, *Bull. Seismol. Soc. Am.*, *92*, 1841–1846.

Harris, R. A., and P. Segall (1987), Detection of a locked zone at depth on the Parkfield, California, segment of the San Andreas Fault, *J. Geophys. Res.*, *92*, 7945–7962.

Heki, K., S. Miyazake, and H. Tsuji (1997), Silent fault slip following an interplate thrust earthquake at the Japan trench, *Nature*, *386*, 595–598.

Helmstetter, A. (2003), Is earthquake triggering driven by small earthquakes?, *Phys. Rev. Lett.*, *91*(5), doi:10.1103/PhysRevLett.91.058501.

Helmstetter, A., and D. Sornette (2002), Subcritical and supercritical regimes in epidemic models of earthquake aftershocks, *J. Geophys. Res.*, *107*(B10), 2237, doi:10.1029/2001JB001580.

Helmstetter, A., and D. Sornette (2003a), Båth's law derived from the Gutenberg-Richter law and from aftershock properties, *Geophys. Res. Lett.*, *30*(20), 2069, doi:10.1029/2003GL018186.

Helmstetter, A., and D. Sornette (2003b), Importance of direct and indirect triggered seismicity in the ETAS model of seismicity, *Geophys. Res. Lett.*, *30*(11), 1576, doi:10.1029/2003GL017670.

Hirata, T. (1989), Fractal dimension of fault systems in Japan: Fractal structure in rock fracture geometry at various scales, *Pure Appl. Geophys.*, *131*, 157–170.

Hirose, H., K. Hirahara, F. Kimata, N. Fujii, and S.-I. Miyazake (1999), A slow thrust slip event following the two 1996 Hyuganada earthquakes beneath the Bungo Channel, southwest Japan, *Geophys. Res. Lett.*, *26*, 3237–3240.

Hyndman, R. D., and D. H. Weichert (1983), Seismicity and rates of relative plate motion on the plate boundaries of western North America, *Geophys. J. R. Astron. Soc.*, *72*, 59–82.

Ihmlé, P. F., and T. H. Jordan (1994), Teleseismic search for slow precursors to large earthquakes, *Science*, *266*, 1547–1551.

Ihmlé, P. F., P. Harabaglia, and T. H. Jordan (1993), Teleseismic detection of a slow precursor to the Great 1989 Macquari Ridge earthquake, *Science*, *261*, 177–182.

Jackson, D. D. (1996), The case for huge earthquakes, *Seismol. Res. Lett.*, *67*(1), 3–5.

Kagan, Y. Y. (1991), Seismic moment distribution, *Geophys. J. Int.*, *106*, 123–134.

Kagan, Y. Y. (1993), Statistics of characteristic earthquakes, *Bull. Seismol. Soc. Am.*, *83*, 7–24.

Kagan, Y. Y. (2002a), Seismic moment distribution revisited: I. Statistical results, *Geophys. J. Int.*, *148*, 520–541.

Kagan, Y. Y. (2002b), Seismic moment distribution revisited: II. Moment conservation principle, *Geophys. J. Int.*, *149*, 731–754.

Kagan, Y. Y., and D. D. Jackson (2000), Probabilistic forecasting of earthquakes, *Geophys. J. Int.*, *143*, 438–453.

Kagan, Y. Y., and L. Knopoff (1991), Stochastic synthesis of earthquake catalogs, *J. Geophys. Res.*, *86*, 2853–2862.

Kagan, Y. Y., and S. Wesnousky (1996), The Gutenberg-Richter or characteristic earthquake distribution, Which is it? Discussion and reply, *Bull. Seismol. Soc. Am.*, *86*, 274–291.

Kanamori, H. (1977), The energy release in great earthquakes, *J. Geophys. Res.*, *82*, 2981–2987.

Kanamori, H., and J. J. Cipar (1974), Focal process of the Great Chilean earthquake May 22, 1960, *Phys. Earth Planet Inter.*, *9*, 128–136.

Kanamori, H., and E. Hauksson (1992), A slow earthquake in the Santa Maria basin, California, *Bull. Seismol. Soc. Am.*, *82*, 2087–2096.

Kanamori, H., and G. Stewart (1976), Mode of strain release along the Gibbs Fracture Zone, Mid-Atlantic Ridge, *Phys. Earth Planet. Inter.*, *11*, 312–332.

Kawaski, I., Y. Kawahara, I. Takata, and N. Kosugi (1985), Mode of seismic moment release at transform faults, *Tectonophysics*, *118*, 313–327.

King, G. C. P., R. S. Stein, and J. B. Rundle (1988), The growth of geological structures by repeated earthquakes: 1. Conceptual framework, *J. Geophys. Res.*, *93*, 13,307–13,318.

Kiratzi, A. A. (1993), A study on the active crustal deformation of the North and East Anatolian fault zones, *Tectonophysics*, *225*, 191–203.

Kisslinger, C., and L. M. Jones (1991), Properties of aftershock sequences in southern California, *J. Geophys. Res.*, *96*, 11,947–11,958.

Knopoff, L. (1964), Statistics of earthquakes in southern California, *Bull. Seismol. Soc. Am.*, *54*, 1871–1873.

Langenhorst, A. R., and E. A. Okal (2002), Correlation of beta-value with spreading rate for strike-slip earthquakes of the mid-oceanic ridge system, in *Plate Boundary Zones*, *Geodyn. Ser.*, vol. 30, edited by S. Stein and J. T. Freymueller, pp. 191–202, AGU, Washington, D. C.

Langer, J. S., J. M. Carlson, C. R. Myers, and B. E. Shaw (1996), Slip complexity in dynamic models of earthquake faults, *Proc. Natl. Acad. Sci. U.S.A.*, *93*, 3825–3829.

Ligi, M., E. Bonatti, L. Gasperini, and A. N. Poliakov (2002), Oceanic broad multifault transform plate boundaries, *Geology*, *30*(1), 11–14.

Lilwall, R., and R. Kirk (1985), OBS observations on the Charlie Gibbs Fracture Zone, *Geophys. J. R. Astron. Soc.*, *80*, 195–208.

Linde, A. T., M. T. Gladwin, M. J. Johnson, R. L. Gwyther, and R. G. Bilham (1996), A slow earthquake sequence on the San Andreas Fault, *Nature*, *383*, 65–68.

Lindh, A. G., and D. M. Boore (1981), Control of rupture by fault geometry during the 1966 Parkfield earthquake, *Bull. Seismol. Soc. Am.*, *71*, 95–116.

Mai, P. M., and G. Beroza (2000), Source scaling properties from finite-fault rupture models, *Bull. Seismol. Soc. Am.*, *90*, 604–615.

Main, I. G., and P. W. Burton (1984), Information theory and the earthquake frequency-magnitude distribution, *Bull. Seismol. Soc. Am.*, *74*, 1409–1426.

McGuire, J. J., and T. H. Jordan (2000), Further evidence for the compound nature of slow earthquakes: The Prince Edward Island earthquake of April 28, 1997, *J. Geophys. Res.*, *105*, 7819–7827.

McGuire, J. J., P. F. Ihmlé, and T. H. Jordan (1996), Time-domain observations of a slow precursor to the 1994 Romache Transform earthquake, *Science*, *274*, 82–85.

McGuire, J. J., T. H. Jordan, and J. Lin (2002a), Complexities of transform fault plate boundaries in the oceans, in *Plate Boundary Zones*, *Geodyn. Ser.*, vol. 30, edited by S. Stein and J. T. Freymueller, pp. 219–241, AGU, Washington, D. C.

McGuire, J. J., L. Zhao, and T. H. Jordan (2002b), Predominance of unilateral rupture for a global catalog of large earthquakes, *Bull. Seismol. Soc. Am.*, *92*, 3309–3317.

Miller, M. M., T. Melbourne, D. J. Johnson, and W. Q. Sumner (2002), Periodic slow earthquakes from the Cascadia subduction zone, *Science*, *295*, 2423.

Molnar, P. (1979), Earthquake recurrence intervals and plate tectonics, *Bull. Seismol. Soc. Am.*, *69*, 115–133.

Muller, J. (1983), Earthquake source parameters, seismicity, and tectonics of North Atlantic transform faults, Ph.D. thesis, Mass. Inst. of Technol., Cambridge.

Nadeau, R., and L. R. Johnson (1998), Seismological studies at Parkfield. vi: Moment release rates and estimates of source parameters for small repeating earthquakes, *Bull. Seismol. Soc. Am.*, *88*, 790–814.

Ogata, Y. (1983), Estimation of the parameters in the modified Omori formula for aftershock frequencies by maximum likelihood procedure, *J. Phys. Earth*, *31*, 115–124.

Ogata, Y. (1988), Statistical models for earthquake occurrence and residual analysis for point processses, *J. Am. Stat. Assoc.*, *83*, 9–27.

O'Hanley, D. S., J. V. Chernosky, and F. J. Wicks (1989), The stability of lizardite and chrysotile, *Can. Mineral.*, *27*, 483–493.

Okal, E. A., and A. R. Langenhorst (2000), Seismic properties of the Eltanin Transform System, South Pacific, *Phys. Earth Planet. Inter.*, *119*, 185–208.

Okal, E. A., and S. Stein (1987), The 1942 Southwest Indian Ocean Ridge earthquake: Largest ever recorded on an oceanic transform, *Geophys. Res. Lett.*, *14*, 147–150.

Okal, E. A., and L. M. Stewart (1982), Slow earthquakes along oceanic fracture zones: evidence for asthenospheric flow away from hotspots?, *Earth Planet. Sci. Lett.*, *57*, 75–87.

Oppenheimer, D., et al. (1993), The Cape Mendocino, California, earthquakes of April 1992: Subduction at the triple junction, *Science*, *261*, 433–438.
Ouilion, G., C. Castaing, and D. Sornette (1996), Hierarchical geometry of faulting, *J. Geophys. Res.*, *101*, 5477–5487.
Pegler, G., and S. Das (1996), Analysis of the relationship between seismic moment and fault length for large crustal strike-slip earthquakes between 1977–92, *Geophys. Res. Lett.*, *23*, 905–908.
Pinkston, J., and S. H. Kirby (1982), Experimental deformation of dunite under conditions appropriate to the lithosphere, *Eos Trans. AGU*, *63*, 1094.
Pockalny, R., R. Detrick, and P. Fox (1988), Morphology and tectonics of the Kane transform from Sea Beam bathymetry data, *J. Geophys. Res.*, *93*, 3907–3939.
Pockalny, R. A., P. J. Fox, D. J. Fornari, K. C. Macdonald, and M. R. Perfit (1997), Tectonic reconstruction of the Clipperton and Siqueiros Fracture Zones: Evidence and consequences of plate motion change for the last 3 Myr, *J. Geophys. Res.*, *102*, 3167–3181.
Power, W. L., and T. E. Tullis (1995), A review of the fractal character of natural fault surfaces with implications for friction and the evolution of fault zones, in *Fractals in the Earth Sciences*, edited by P. Lapointe and C. Barton, pp. 89–105, Plenum, New York.
Reasenberg, P. A., and L. M. Jones (1989), Earthquake hazard after a mainshock in California, *Science*, *243*, 1173–1176.
Reinen, L. A. (2000a), Slip styles in a spring-slider model with a laboratory-derived constitutive law for serpentinite, *Geophys. Res. Lett.*, *27*, 2037–2040.
Reinen, L. A. (2000b), Seismic and aseismic slip indicators in serpentinite gouge, *Geology*, *28*(2), 135–138.
Reinen, L. A., J. D. Weeks, and T. E. Tullis (1994), The frictional behavior of lizardite and antigorite serpentinites: Experiments, constitutive models, and implications for natural faults, *Pure Appl. Geophys.*, *143*, 317–385.
Rice, J. R. (1993), Spatiotemporal complexity of slip on a fault, *J. Geophys. Res.*, *98*, 9885–9907.
Romanowicz, B. (1992), Strike-slip earthquakes on quasi-vertical transcurrent faults: Inferences for general scaling relations, *Geophys. Res. Lett.*, *19*(5), 481–484.
Romanowicz, B. (1994), Comment on "A reappraisal of large earthquake scaling" by C. Scholz, *Bull. Seismol. Soc. Am.*, *84*, 1675–1676.
Romanowicz, B., and L. J. Ruff (2002), On moment-length scaling of large strike slip earthquakes and the strength of faults, *Geophys. Res. Lett.*, *29*(12), 1604, doi:10.1029/2001GL014479.
Rundquist, D., and P. Sobolev (2002), Seismicity of mid-ocean ridges and its geodynamic implications: A review, *Earth Sci. Rev.*, *58*, 143–161.
Sacks, I., S. Suyehiro, A. T. Linde, and J. A. Snoke (1978), Slow earthquakes and stress redistribution, *Nature*, *275*, 599–602.
Sammis, C. G., and J. R. Rice (2001), Repeating earthquakes as low-stress-drop events at a border between locked and creeping fault patches, *Bull. Seismol. Soc. Am.*, *91*, 532–537.
Scholz, C. H. (1982), Scaling laws for large earthquakes: Consequences for physical models, *Bull. Seismol. Soc. Am.*, *72*, 1–14.
Scholz, C. H. (1994a), A reappaisal of large earthquake scaling, *Bull. Seismol. Soc. Am.*, *84*, 215–218.
Scholz, C. H. (1994b), Reply to comments on "A reappaisal of large earthquake scaling" by C. Scholz, *Bull. Seismol. Soc. Am.*, *84*, 1677–1678.
Scholz, C. H. (2002), *The Mechanics of Earthquakes and Faulting*, 2nd ed., Cambridge Univ. Press, New York.
Schulz, S. S., G. M. Mavko, R. O. Burford, and W. D. Stuart (1982), Long-term fault creep observations in central California, *J. Geophys. Res.*, *87*, 6977–6982.
Schwartz, D. (1996), The case against huge earthquakes, *Seismol. Res. Lett.*, *67*(3), 3–5.
Schwartz, D. P., and K. J. Coppersmith (1984), Fault behavior and characteristic earthquakes: Examples from the Wasatch and San Andreas fault zones, *J. Geophys. Res.*, *89*, 5681–5698.
Shaw, B. E., and J. R. Rice (2000), Existence of continuum complexity in the elastodynamics of repeated fault ruptures, *J. Geophys. Res.*, *105*, 791–810.
Shaw, B. E., and C. H. Scholz (2001), Slip-length scaling in large earthquakes: Observations and theory and implications for earthquake physics, *Geophys. Res. Lett.*, *28*, 2991–2994.
Shimazaki, K. (1986), Small and large earthquakes: The effects of the thickness of the seismogenic layer and the free surface, in *Earthquake Source Mechanics*, *Geophys. Monogr. Ser.*, vol. 37, edited by S. Das et al., pp. 209–216, AGU, Washington, D. C.
Sibson, R. H. (1983), Continental fault structure and the shallow earthquake source, *J. Geol. Soc. London*, *140*, 741–767.
Sleep, N. H. (1975), Formation of the oceanic crust: Some thermal constraints, *J. Geophys. Res.*, *80*, 4037–4042.
Smith, D. K., and T. H. Jordan (1988), Seamount statistics in the Pacific Ocean, *J. Geophys. Res.*, *93*, 2899–2918.
Smith, W. H. F., and D. T. Sandwell (1997), Global seafloor topography from satellite altimetry and ship depth soundings, *Science*, *277*, 1957–1962.
Sobolev, P., and D. V. Rundquist (1999), Seismicity of oceanic and continental rifts—A geodynamic approach, *Phys. Earth Planet. Inter.*, *111*, 253–266.
Solomon, S. C., and N. C. Burr (1979), The relationship of source parameters of ridge-crest and transform earthquakes to the thermal structure of oceanic lithosphere, *Tectonophysics*, *55*, 107–126.
Stein, R. C., and T. C. Hanks (1998), $M \geq 6$ earthquakes in southern California during the twentieth century: No evidence for a seismicity or moment deficit, *Bull. Seismol. Soc. Am.*, *88*, 635–652.
Stein, S., and A. Pelayo (1991), Seismological constraints on stress in the oceanic lithosphere, *Philos. Trans. R. Soc. London, Ser. A*, *337*, 53–72.
Stesky, R. M., W. F. Brace, D. K. Riley, and P.-Y. F. Robin (1974), Friction in faulted rock at high temperature and pressure, *Tectonophysics*, *23*, 177–203.
Stirling, M. W., S. G. Wesnousky, and K. Shimazaki (1996), Fault trace complexity, cumulative slip, and the shape of the magnitude-frequency distribution for strike-slip faults: A global survey, *Geophys. J. Int.*, *124*, 833–868.
Stoddard, P. R. (1992), On the relation between transform fault resistance and plate motion, *J. Geophys. Res.*, *97*, 17,637–17,650.
Thatcher, W. (1990), Present-day crustal movements and the mechanics of cyclic deformation, in San Andreas Fault System, California, edited by R. Wallace, *U. S. Geol. Surv. Prof. Pap.*, *1515*, 189–205.
Thurber, C., and R. Sessions (1998), Assessment of creep events as potential earthquake precursors: Application to the creeping section of the San Andreas Fault, California, *Pure Appl. Geophys.*, *152*, 685–705.
Trehu, A., and S. Solomon (1983), Earthquakes in the Orozco Transform Zone: Seismicity, source mechanism, and tectonics, *J. Geophys. Res.*, *88*, 8203–8225.
Tucholke, B. E., and J. Lin (1994), A geological model for the structure of ridge segments in slow-spreading ocean crust, *J. Geophys. Res.*, *99*, 11,937–11,958.
Turcotte, D. L. (1986), A fractal model for crustal deformation, *Tectonophysics*, *132*, 261–269.
Turcotte, D. L., and G. Schubert (2001), *Geodynamics, Application of Continuum Physics to Geological Problems*, Cambridge Univ. Press, New York.
Utsu, T. (1961), A statistical study on the occurrence of aftershocks, *Geophys. Mag.*, *30*, 521–605.
Utsu, T. (1969), Aftershocks and earthquake statistics, I, Some parameters which characterize an aftershock sequence and their interaction, *J. Fac. Sci. Hokkaido Univ., Ser.*, *7*(3), 129–195.
Wald, D., T. Heaton, and K. Hudnut (1996), The slip history of the 1994 Northridge, California, earthquake determined from strong-motion, teleseismic, GPS, and leveling data, *Bull. Seismol. Soc. Am.*, *86*, S49–S70.
Waldhauser, F., and W. L. Ellsworth (2002), Fault structure and mechanics of the Hayward Fault, California, from double-difference earthquake locations, *J. Geophys. Res.*, *107*(B3), 2054, doi:10.1029/2000JB000084.
Wang, J.-H., and S.-S. Ou (1998), On scaling of earthquake faults, *Bull. Seismol. Soc. Am.*, *88*, 758–766.
Ward, S. N. (1997), More on m_{max}, *Bull. Seismol. Soc. Am.*, *87*, 1199–1208.
Wesnousky, S. G. (1990), Seismicity as a function of cumulative geologic offset: Some observations from southern California, *Bull. Seismol. Soc. Am.*, *80*, 1374–1381.
Wesnousky, S. G. (1994), The Gutenberg-Richter or characteristic earthquake distribution, which is it?, *Bull. Seismol. Soc. Am.*, *84*, 1940–1959.
Wesson, R. L. (1988), Dynamics of fault creep, *J. Geophys. Res.*, *93*, 8929–8951.
Wiemer, S., and M. Wyss (2000), Minimum magnitude of completeness in earthquake catalogs: Examples from Alaska, the western United States, and Japan, *Bull. Seismol. Soc. Am.*, *90*, 859–869.
Wiens, D. A., and S. Stein (1983), Age dependenc of oceanic intraplate seismicity and implications for lithospheric evolution, *J. Geophys. Res.*, *88*, 6455–6468.
Wilcock, W., G. Purdy, and S. Solomon (1990), Microearthquake evidence for extension across the Kane Transform Fault, *J. Geophys. Res.*, *95*, 15,439–15,462.
Yamanaka, Y., and K. Shimazaki (1990), Scaling relationship between the number of aftershocks and the size of the main shock, *J. Phys. Earth*, *38*, 305–324.
Yeats, R. S., C. R. Allen, and K. E. Sieh (1997), *The Geology of Earthquakes*, Oxford Univ. Press, New York.

M. S. Boettcher, MIT/WHOI Joint Program, Woods Hole Oceanographic Institution, Woods Hole, MA 02543, USA. (margaret@whoi.edu)
T. H. Jordan, Department of Earth Sciences, University of Southern California, Los Angeles, CA 90089-0740, USA. (tjordan@usc.edu)